particles

IMPACT FACTOR 1.7

CITESCORE 3.2

Article

Extensions of the Variational Method with an Explicit Energy Functional for Nuclear Matter with Spin-Orbit Force

Kento Kitanaka, Toshiya Osuka, Tetsu Sato, Hayate Ichikawa and Masatoshi Takano

Special Issue

Selected Papers from the 22nd International Conference on Recent Progress in Many-Body Theories

Edited by

Prof. Dr. Armen Sedrakian, Prof. Dr. Morten Hjorth-Jensen, Prof. Dr. Takashi Nakatsukasa, Prof. Dr. Gerardo Ortiz and Dr. Heidi Reinholz

MDPI

https://doi.org/10.3390/particles8010011

particles

MDPI

Article

Extensions of the Variational Method with an Explicit Energy Functional for Nuclear Matter with Spin-Orbit Force

Kento Kitanaka [1,*], Toshiya Osuka [1,*], Tetsu Sato [1], Hayate Ichikawa [1] and Masatoshi Takano [1,2]

[1] Department of Physics and Applied Physics, Waseda University, Tokyo 169-8555, Japan; takanom@waseda.jp (M.T.)
[2] Institute for Advanced Theoretical and Experimental Physics, Waseda University, Tokyo 169-8555, Japan
* Correspondence: k-kent10654@ruri.waseda.jp (K.K.); momo.07-27-h21@ruri.waseda.jp (T.O.)

Abstract: Two extensions of the variational method with explicit energy functionals (EEFs) with respect to the spin-orbit force were performed. In this method, the energy per nucleon of nuclear matter is explicitly expressed as a functional of various two-body distribution functions, starting from realistic nuclear forces. The energy was then minimized by solving the Euler–Lagrange equation for the distribution functions derived from the EEF. In the first extension, an EEF of symmetric nuclear matter at zero temperature was constructed using the two-body central, tensor, and spin-orbit nuclear forces. The energy per nucleon calculated using the Argonne v8′ two-body nuclear potential was found to be lower than those calculated using other many-body methods, implying that the energy contribution caused by the spin-orbit correlation, whose relative orbital angular momentum operator acts on other correlations, is necessary. In a subsequent extension, the EEF of neutron matter at zero temperature, including the spin-orbit force, was extended to neutron matter at finite temperatures using the method by Schmidt and Pandharipande. The thermodynamic quantities of neutron matter calculated using the Argonne v8′ nuclear potential were found to be reasonable and self-consistent.

Keywords: nuclear matter; variational method; nuclear force

Academic Editor: Armen Sedrakian

Received: 31 December 2024
Revised: 28 January 2025
Accepted: 4 February 2025
Published: 7 February 2025

Citation: Kitanaka, K.; Osuka, T.; Sato, T.; Ichikawa, H.; Takano, M. Extensions of the Variational Method with an Explicit Energy Functional for Nuclear Matter with Spin-Orbit Force. *Particles* **2025**, *8*, 11. https://doi.org/10.3390/particles8010011

1. Introduction

The equation of state (EOS) of infinite, uniform nuclear matter is particularly important in the fields of nuclear physics and astrophysics. The structure of isolated neutron stars is governed by a cold nuclear matter EOS [1]. The EOS of nuclear matter at finite temperatures is essential for studying core collapse supernova (CCSN) explosions [2] and binary neutron star mergers [3].

Theoretical calculations are required to determine the EOS because it is difficult to complete a nuclear EOS. Specifically, the energy per nucleon of nuclear matter has been investigated using various quantum many-body techniques, starting from the so-called modern two-body nuclear potential, which precisely reproduces the experimental two-nucleon scattering data, and the three-body nuclear potential [4].

A notable example is the nuclear matter EOS by Akmal, Pandharipande, and Ravenhall (APR) [5], which is frequently cited as a representative example of a nuclear matter EOS. This EOS is based on the Argonne V18 modern two-body nuclear potential [6] and Urbana IX three-body nuclear potential [7,8]. Then, the expectation value of the nuclear Hamiltonian with the Jastrow wave function is expanded into cluster terms [9], which are partially resummed using the Fermi hypernetted chain method [4]. Finally, the energy per nucleon is minimized with respect to the correlation functions in the Jastrow wave function.

The EOS by APR was subsequently extended to nuclear matter at finite temperatures [10] with the method by Schmidt and Pandharipande [11].

Furthermore, quantum many-body theories have been developed to obtain the exact solution of the energy eigenvalue problem, starting from a realistic nuclear Hamiltonian. Such studies include the Green's function Monte Carlo and auxiliary field diffusion Monte Carlo (AFDMC) methods [12].

In recent years, nuclear forces based on the chiral effective field theory have also been actively studied [13], and nuclear EOSs utilizing these forces have also been the subject of intensive research [14]. However, nuclear forces based on the chiral effective field theory have relatively large uncertainties in the high-density region, which poses difficulties when considering their applications to compact stars or CCSNe.

In general, nuclear EOSs applicable to CCSN numerical simulations must cover an extremely wide range of densities $\rho_{\rm B}$, temperatures T, and proton fractions $Y_{\rm p}$. It is difficult to perform quantum many-body calculations for nuclear matter at various values of $(\rho_{\rm B}, T, Y_{\rm p})$. Consequently, in the early stages of research, nuclear EOSs applicable to CCSNe were limited to those based on phenomenological theories, such as the EOS by Lattimer and Swesty [15] and that by Shen et al. [16].

Under these circumstances, we have developed a nuclear EOS applicable to CCSNe based on realistic nuclear forces [17]. The starting point was the same Hamiltonian and wave function as in the APR EOS; however, only the lowest-order cluster terms were retained. Furthermore, the healing distance was incorporated into the correlation functions in the Jastrow wave function to obtain an EOS close to that of the APR. It is important to note that both uniform and non-uniform phases must be treated. The non-uniform phase is calculated by a single-nucleus approximation using the Thomas–Fermi approximation [17] or a multi-component approximation [18]. The constructed nuclear EOS has been applied to numerical simulations of CCSNe and binary neutron star mergers. Furthermore, it has been extended to include hyperon mixing [19] and phase transitions to quark phases at high densities [20].

However, as mentioned previously, the EOS was constructed using the lowest-order cluster approximation. To obtain a more reliable EOS, it is necessary to appropriately incorporate higher-order effects.

Therefore, we investigated a variational method using an explicit energy functional (EEF) [21]. In this method, the expectation value of the nuclear Hamiltonian for uniform nuclear matter is expressed as an explicit functional of various two-body distribution functions. The Euler–Lagrange equations are then derived directly from the EEF and solved numerically to obtain the fully minimized energy. The expectation value of the two-body nuclear potential is expressed exactly using the two-body distribution function. For the kinetic energy caused by the correlation between nucleons, the EEF is constructed to include the main parts of the cluster terms by temporarily assuming a Jastrow wave function. Furthermore, an EEF is constructed to guarantee necessary conditions on various structure functions.

This variational method has been proposed and improved, including extensions of the theory to treat the two-body tensor force and the three-body nuclear force. This theory has also been extended to nuclear matter at a finite temperature [22]. Furthermore, in a previous study [23], we extended the EEF to treat the two-body spin-orbit force for pure neutron matter (PNM), and the energies obtained with and without the three-body force were in good agreement with those obtained using the AFDMC method [24].

This paper presents two extensions of the variational method. In Section 2, an extension of the EEF for symmetric nuclear matter (SNM) is presented to incorporate the two-body spin-orbit force, and the numerical results are discussed. In Section 3, an extension

of the EEF for PNM at zero temperature with the two-body central, tensor, and spin-orbit forces to PNM at a finite temperature by following the method of Schmidt and Pandharipande is presented. Finally, Section 4 provides a summary and our concluding remarks.

2. Explicit Energy Functional of Symmetric Nuclear Matter at Zero Temperature

2.1. Construction of the Energy Functional Including Spin-Orbit Forces

In this subsection, we construct the explicit energy functional (EEF) of SNM at zero temperature using spin-orbit forces. We begin with the following Hamiltonian:

$$H = -\sum_{i=1}^{N} \frac{\hbar^2}{2m} \nabla_i^2 + \sum_{i>j} V_{ij}, \tag{1}$$

where m is the mass of a nucleon, N is the number of nucleons, and V_{ij} is the potential of the two-body nuclear force. In this study, we employ the Argonne v8′ potential [25]:

$$V_{ij} = \sum_{t=0}^{1} \sum_{s=0}^{1} \left[V_{Cts}(r_{ij}) + V_{Tt}(r_{ij}) S_{Tij} + V_{SOt}(r_{ij}) (\boldsymbol{s} \cdot \boldsymbol{L}_{ij}) \right] P_{tsij}, \tag{2}$$

where t and s denote the two-nucleon total isospin and spin, respectively, and $V_{Cts}(r)$, $V_{Tt}(r)$, and $V_{SOt}(r)$ are the central, tensor, and spin-orbit components of the two-body nuclear potential, respectively. Furthermore, P_{tsij} is the spin-isospin projection operator, S_{Tij} is the tensor operator, $\boldsymbol{s}$ is the two-nucleon spin operator, and $\boldsymbol{L}_{ij}$ is the relative orbital angular operator for the nucleon pair (i, j).

For the above Hamiltonian, we construct an EEF per nucleon for SNM with a given nucleon number density ρ. For this purpose, we first introduce the following functions:

$$F_{ts}(r_{12}) = \Omega^2 \sum_{isospin} \sum_{spin} \int \Psi^\dagger(x_1, x_2, \ldots, x_N) P_{ts12} \Psi^\dagger(x_1, x_2, \ldots, x_N) d\boldsymbol{r}_3 d\boldsymbol{r}_4 \ldots d\boldsymbol{r}_N, \tag{3}$$

$$F_{Tt}(r_{12}) = \Omega^2 \sum_{isospin} \sum_{spin} \int \Psi^\dagger(x_1, x_2, \ldots, x_N) S_{T12} P_{t112} \Psi^\dagger(x_1, x_2, \ldots, x_N) d\boldsymbol{r}_3 d\boldsymbol{r}_4 \ldots d\boldsymbol{r}_N, \tag{4}$$

$$F_{SOt}(r_{12}) = \Omega^2 \sum_{isospin} \sum_{spin} \int \Psi^\dagger(x_1, x_2, \ldots, x_N) (\boldsymbol{s} \cdot \boldsymbol{L}_{12}) P_{t112} \Psi^\dagger(x_1, x_2, \ldots, x_N) d\boldsymbol{r}_3 d\boldsymbol{r}_4 \ldots d\boldsymbol{r}_N. \tag{5}$$

Here , Ω is the volume of the system, and x_i is the coordinate of the ith nucleon, including the space coordinate $\boldsymbol{r}_i$, the spin coordinate, and the isospin coordinate. $\sum_{isospin}$ and $\sum_{spin}$ represent the sums of the isospin and spin coordinates, respectively.

Furthermore, we introduce the auxiliary functions—the intrinsically central distribution functions $F_{Cts}(r)$, dressed tensor correlation functions $g_{Tt}(r)$, and dressed spin-orbit correlation functions $g_{SOt}(r)$—which are defined as the solutions of the following equations:

$$F_{ts}(r) = F_{Cts}(r) + 8s[g_{Tt}(r)]^2 F_{Fts}(r) + \frac{2}{3} s[g_{SOt}(r)]^2 F_{qFts}(r), \tag{6}$$

$$F_{Tt}(r) = 16\left[\sqrt{F_{Ct1}(r) F_{Ft1}(r)}\, g_{Tt}(r) - [g_{Tt}(r)]^2 F_{Ft1}(r) \right] - \frac{2}{3} [g_{SOt}(r)]^2 F_{qFt1}(r), \tag{7}$$

$$F_{SOt}(r) = -24[g_{Tt}(r)]^2 F_{Ft1}(r) + \frac{4}{3}\left[\sqrt{\frac{F_{Ct1}(r)}{F_{Ft1}(r)}}\, g_{Tt}(r) - \frac{[g_{Tt}(r)]^2}{4} - g_{Tt}(r) g_{SOt}(r) \right] F_{qFt1}(r). \tag{8}$$

Here, $F_{Fts}(r)$ is $F_{ts}(r)$ in the case of the non-interacting Fermi gas and is given by

$$F_{Fts}(r) = \frac{(2t+1)(2s+1)}{16} \left\{ 1 - (-1)^{t+s} [l(k_F r)]^2 \right\}, \tag{9}$$

with $l(x) = 3j_1(x)/x$ being the Slater function. Furthermore, $F_{\mathrm{qF}ts}(r)$ is given by

$$\begin{aligned} F_{\mathrm{qF}ts}(r_{12}) &= \Omega^2 \sum_{isospin} \sum_{spin} \int \Phi_{\mathrm{F}}^{\dagger}(x_1, x_2, \ldots, x_N) |\boldsymbol{L}_{12}|^2 P_{ts12} \Phi_{\mathrm{F}}(x_1, x_2, \ldots, x_N) d\boldsymbol{r}_3 d\boldsymbol{r}_4 \ldots d\boldsymbol{r}_N \\ &= \frac{(2t+1)(2s+1)}{16} \left[\frac{(k_{\mathrm{F}} r_{12})^2}{5} + (-1)^{t+s} 9 j_2(k_{\mathrm{F}} r_{12}) \frac{j_1(k_{\mathrm{F}} r_{12})}{k_{\mathrm{F}} r_{12}} \right], \end{aligned} \tag{10}$$

where $\Phi_{\mathrm{F}}(x_1, x_2, \ldots, x_N)$ is the wave function of the non-interacting Fermi gas.

In addition, the following structure functions are necessary to construct the EEF:

$$S_{\mathrm{c}1}(k) = \frac{1}{N} \left\langle \left| \sum_{i=1}^{N} \exp(i\boldsymbol{k} \cdot \boldsymbol{r}_i) \right|^2 \right\rangle = 1 + S_{11}(k) + S_{10}(k) + S_{01}(k) + S_{00}(k) \geq 0, \tag{11}$$

$$S_{\mathrm{c}2}(k) = \frac{1}{3N} \left\langle \left| \sum_{i=1}^{N} \boldsymbol{\sigma}_i \exp(i\boldsymbol{k} \cdot \boldsymbol{r}_i) \right|^2 \right\rangle = 1 + \frac{S_{11}(k)}{3} - S_{10}(k) + \frac{S_{01}(k)}{3} - S_{00}(k) \geq 0, \tag{12}$$

$$S_{\mathrm{c}3}(k) = \frac{1}{3N} \left\langle \left| \sum_{i=1}^{N} \boldsymbol{\tau}_i \exp(i\boldsymbol{k} \cdot \boldsymbol{r}_i) \right|^2 \right\rangle = 1 + \frac{S_{11}(k)}{3} + \frac{S_{10}(k)}{3} - S_{01}(k) - S_{00}(k) \geq 0, \tag{13}$$

$$S_{\mathrm{c}4}(k) = \frac{1}{9N} \left\langle \left| \sum_{i=1}^{N} \boldsymbol{\tau}_i \boldsymbol{\sigma}_i \exp(i\boldsymbol{k} \cdot \boldsymbol{r}_i) \right|^2 \right\rangle = 1 + \frac{S_{11}(k)}{9} - \frac{S_{10}(k)}{3} - \frac{S_{01}(k)}{3} + S_{00}(k) \geq 0. \tag{14}$$

Here, $S_{ts}(k)$ represents the Fourier transforms of $F_{ts}(r)$, given by

$$S_{ts}(k) = 4\pi\rho \int_0^{\infty} [F_{ts}(r) - F_{ts}(\infty)] j_0(kr) r^2 dr. \tag{15}$$

In addition, $S_{\mathrm{cT}n}(k)$ are given by

$$S_{\mathrm{cT}1}(k) = \frac{1}{Nk^2} \left\langle \left| \sum_{i=1}^{N} (\boldsymbol{\sigma}_i \cdot \boldsymbol{k}) \exp(i\boldsymbol{k} \cdot \boldsymbol{r}_i) \right|^2 \right\rangle = S_{\mathrm{c}2}(k) - \frac{S_{\mathrm{T}1}(k)}{3} - \frac{S_{\mathrm{T}0}(k)}{3} \geq 0, \tag{16}$$

$$S_{\mathrm{cT}2}(k) = \frac{1}{2Nk^2} \left\langle \left| \sum_{i=1}^{N} (\boldsymbol{\sigma}_i \times \boldsymbol{k}) \exp(i\boldsymbol{k} \cdot \boldsymbol{r}_i) \right|^2 \right\rangle = S_{\mathrm{c}2}(k) + \frac{S_{\mathrm{T}1}(k)}{6} + \frac{S_{\mathrm{T}0}(k)}{6} \geq 0, \tag{17}$$

$$S_{\mathrm{cT}3}(k) = \frac{1}{Nk^2} \left\langle \left| \sum_{i=1}^{N} \boldsymbol{\tau}_i (\boldsymbol{\sigma}_i \cdot \boldsymbol{k}) \exp(i\boldsymbol{k} \cdot \boldsymbol{r}_i) \right|^2 \right\rangle = S_{\mathrm{c}4}(k) - \frac{S_{\mathrm{T}1}(k)}{9} + \frac{S_{\mathrm{T}0}(k)}{3} \geq 0, \tag{18}$$

$$S_{\mathrm{cT}4}(k) = \frac{1}{2Nk^2} \left\langle \left| \sum_{i=1}^{N} \boldsymbol{\tau}_i (\boldsymbol{\sigma}_i \times \boldsymbol{k}) \exp(i\boldsymbol{k} \cdot \boldsymbol{r}_i) \right|^2 \right\rangle = S_{\mathrm{c}4}(k) + \frac{S_{\mathrm{T}1}(k)}{18} - \frac{S_{\mathrm{T}0}(k)}{6} \geq 0, \tag{19}$$

with $S_{\mathrm{T}t}(k)$ being

$$S_{\mathrm{T}t}(k) = 4\pi\rho \int_0^{\infty} F_{\mathrm{T}t}(r) j_2(kr) r^2 dr. \tag{20}$$

The following structure functions are also necessary:

$$S_{\mathrm{SO}t}(k) = 4\pi\rho \int_0^{\infty} F_{\mathrm{SO}t}(r) \frac{j_1(kr)}{k_{\mathrm{F}} r} r^2 dr. \tag{21}$$

Using these distribution functions and structure functions, we express the energy per nucleon of SNM at zero temperature as follows:

$$\frac{E}{N} = \frac{3}{5} E_{\mathrm{F}} + \frac{E_{\mathrm{V}}}{N} + \frac{E_{\mathrm{TF}}}{N} + \frac{E_{\mathrm{TS}}}{N} + \frac{E_{\mathrm{TN}}}{N}. \tag{22}$$

Here, $E_{\mathrm{F}} = \hbar^2 k_{\mathrm{F}}^2/2m$ is the Fermi energy, and $k_{\mathrm{F}} = \left(3\pi^2\rho/2\right)^{1/3}$ is the Fermi wave number. The second term on the right-hand side of Equation (22) is the potential energy, which is expressed as follows:

$$\frac{E_{\mathrm{V}}}{N} = 2\pi\rho \int_0^\infty \sum_{t=0}^{1} \left[\sum_{s=0}^{1} F_{ts}(r) V_{\mathrm{C}ts}(r) + F_{\mathrm{T}t}(r) V_{\mathrm{T}t}(r) + F_{\mathrm{SO}t}(r) V_{\mathrm{SO}t}(r) \right] r^2 dr. \tag{23}$$

This is the exact expression for the potential energy expectation value. The remaining terms on the right-hand side of Equation (22) represent the kinetic energy caused by the correlation between nucleons. In particular, the third term on the right-hand side of Equation (22), E_{TF}/N, is expressed using the auxiliary functions $F_{\mathrm{C}ts}(r)$, $g_{\mathrm{T}t}(r)$, and $g_{\mathrm{SO}t}(r)$:

$$\begin{aligned} \frac{E_{\mathrm{TF}}}{N} &= \frac{\pi\hbar^2\rho}{2m} \int_0^\infty \sum_{t=0}^{1} \sum_{s=0}^{1} F_{\mathrm{C}ts}(r) \left[\frac{1}{F_{\mathrm{C}ts}(r)} \frac{dF_{\mathrm{C}ts}(r)}{dr} - \frac{1}{F_{\mathrm{F}ts}(r)} \frac{dF_{\mathrm{F}ts}(r)}{dr} \right]^2 r^2 dr \\ &\quad + \frac{2\pi\hbar^2\rho}{m} \int_0^\infty \sum_{t=0}^{1} \left[8 \left\{ \left[\frac{dg_{\mathrm{T}t}(r)}{dr} \right]^2 + \frac{6}{r^2} [g_{\mathrm{T}t}(r)]^2 \right\} F_{\mathrm{F}ts}(r) \right. \\ &\quad \left. + \frac{2}{3} \left[\frac{dg_{\mathrm{SO}t}(r)}{dr} \right]^2 F_{\mathrm{qF}t1}(r) \right] r^2 dr. \end{aligned} \tag{24}$$

In contrast, the next term, E_{TS}/N, is expressed with the structure functions

$$\begin{aligned} \frac{E_{\mathrm{TS}}}{N} &= -\frac{\hbar^2}{16\pi^2 m\rho} \int_0^\infty \sum_{n=1,3} n \frac{[S_{\mathrm{c}n}(k) - 3 + 2S_{\mathrm{cF}}(k)][S_{\mathrm{c}n}(k) - S_{\mathrm{cF}}(k)]^2}{S_{\mathrm{c}n}(k)/S_{\mathrm{cF}}(k)} k^4 dk \\ &\quad - \frac{\hbar^2}{16\pi^2 m\rho} \int_0^\infty \sum_{n=1}^{4} w_n \frac{[S_{\mathrm{cT}n}(k) - 3 + 2S_{\mathrm{cF}}(k)][S_{\mathrm{cT}n}(k) - S_{\mathrm{cF}}(k)]^2}{S_{\mathrm{cT}n}(k)/S_{\mathrm{cF}}(k)} k^4 dk \\ &\quad - \frac{\hbar^2}{16\pi^2 m\rho} \int_0^\infty \sum_{n=1,3} \frac{15}{2} n \frac{[S_{\mathrm{c}n}(k) - S_{\mathrm{SOF}}(k)]}{S_{\mathrm{c}n}(k)/S_{\mathrm{cF}}(k)} [T_{\mathrm{SO}n}(k)]^2 k^4 dk \\ &\quad - \frac{\hbar^2}{16\pi^2 m\rho} \int_0^\infty \sum_{n=2,4} \frac{15}{2} w_n \frac{[S_{\mathrm{cT}n}(k) - S_{\mathrm{SOF}}(k)]}{S_{\mathrm{cT}n}(k)/S_{\mathrm{cF}}(k)} [T_{\mathrm{SO}n}(k)]^2 k^4 dk. \end{aligned} \tag{25}$$

Here, $S_{\mathrm{cF}}(k)$ is the structure function of the non-interacting Fermi gas, which is given by

$$S_{\mathrm{cF}}(k) = \begin{cases} \frac{3k}{4k_{\mathrm{F}}} - \frac{1}{16}\left(\frac{k}{k_{\mathrm{F}}}\right)^3 & \text{for } k \le 2k_{\mathrm{F}} \\ 1 & \text{for } k \ge 2k_{\mathrm{F}}. \end{cases} \tag{26}$$

Furthermore, $S_{\mathrm{SOF}}(k)$ in Equation (25) is given by

$$S_{\mathrm{SOF}}(k) = \frac{5}{3} S_{\mathrm{cF}}(k) - \frac{5}{3} - \frac{25}{12} S_{\mathrm{l1}}(k) + \frac{25}{3} S_{\mathrm{Fa}}(k) + \frac{5}{3} S_{\mathrm{Fb}}(k) \tag{27}$$

with

$$S_{\mathrm{l1}}(k) = 4\pi\rho \int_0^\infty \left[\frac{dl(k_{\mathrm{F}}r)}{dr} \frac{1}{k_{\mathrm{F}}} \right]^2 \frac{j_1(kr)}{kr} r^2 dr, \tag{28}$$

$$S_{\mathrm{Fa}}(k) = 4\pi\rho \int_0^\infty \frac{dl(k_{\mathrm{F}}r)}{dr} \left[\frac{d^2 l(k_{\mathrm{F}}r)}{dr^2} - \frac{1}{r} \frac{dl(k_{\mathrm{F}}r)}{dr} \right] \frac{1}{k_{\mathrm{F}}^2} \frac{j_2(kr)}{kr} \frac{1}{k} r^2 dr, \tag{29}$$

and

$$S_{\mathrm{Fb}} = 4\pi\rho \int_0^\infty l(k_{\mathrm{F}}r) \frac{dl(k_{\mathrm{F}}r)}{dr} j_1(kr) \frac{1}{k} r^2 dr. \tag{30}$$

In addition, we have

$$T_{\mathrm{SO}n}(k) = \begin{cases} S_{\mathrm{SO}1}(k) + S_{\mathrm{SO}0}(k) & n = 1,2 \\ \frac{1}{3} S_{\mathrm{SO}1}(k) - S_{\mathrm{SO}0}(k) & n = 3,4, \end{cases} \tag{31}$$

and $(w_1, w_2, w_3, w_4) = (1, 2, 3, 6)$. The explicit functional form of the last term on the right-hand side of Equation (22), E_{TN}/N, is presented in Appendix A.

The EEF given in Equation (22) is constructed so as to satisfy the following conditions:

(1) The energy per nucleon E/N for SNM is expressed as an explicit functional of $F_{cts}(r)$, $g_{\mathrm{T}t}(r)$, and $g_{\mathrm{SO}t}(r)$ such that the Euler–Lagrange equations are derived directly from the EEF through the variational procedure.

(2) The two-body potential energy per nucleon, E_{V}/N, is expressed exactly.

(3) To express the kinetic energy caused by the correlation between nucleons, we temporarily assume the following Jastrow-type wave function:

$$\Psi(x_1, \ldots, x_N) = \mathrm{Sym}\left[\prod_{i<j} f_{ij}\right] \Phi_{\mathrm{F}}(x_1, \ldots, x_N). \tag{32}$$

Here, Sym[] on the right-hand side of Equation (32) is a symmetrizer with respect to the order of the factors in the product, and f_{ij} is the correlation function between the (i, j) nucleon pair, given by

$$f_{ij} = \sum_{t=0}^{1} \sum_{s=0}^{1} \left[f_{\mathrm{C}ts}(r_{ij}) + s f_{\mathrm{T}t}(r_{ij}) S_{\mathrm{T}ij} + s f_{\mathrm{SO}t}(r_{ij}) (\boldsymbol{s} \cdot \boldsymbol{L}_{ij}) \right] P_{tsij}. \tag{33}$$

Subsequently, the expectation value of the two-body Hamiltonian H with the Jastrow wave function $\Psi(x_1, \ldots, x_N)$ is expanded into cluster terms [9]. Using the cluster terms, the kinetic energy expression derived from the correlations is constructed as follows:

(3a) The two-body cluster terms are included exactly. This is the reason why the auxiliary functions $F_{\mathrm{C}ts}(r)$, $g_{\mathrm{T}t}(r)$, and $g_{\mathrm{SO}t}(r)$ are introduced. When we impose the two-body cluster approximations of $F_{\mathrm{C}ts}(r)$, $g_{\mathrm{T}t}(r)$, and $g_{\mathrm{SO}t}(r)$ as $[f_{\mathrm{C}ts}(r)]^2 F_{\mathrm{F}ts}(r)$, $f_{\mathrm{T}t}(r)$, and $f_{\mathrm{SO}t}(r)$, respectively, E_{TF}/N is reduced to a two-body cluster expression for the kinetic energy caused by the correlation between nucleons, and the right-hand sides of Equations (6)–(8) are reduced to the two-body cluster approximations of $F_{ts}(r)$, $F_{\mathrm{T}t}(r)$, and $F_{\mathrm{SO}t}(r)$, respectively. Note that E_{TF}/N includes the three-body cluster and higher-order cluster terms because the auxiliary functions, originally defined as the solutions to Equations (6)–(8), also include higher-order cluster terms.

(3b) E_{TF}/N is found to be insufficient for representing the main part of the three-body cluster terms caused by the correlations (i.e., the three-body cluster direct terms that are the lowest (third) order in the correlation $h_{ij} = f_{ij} - 1$). In the case of PNM with central correlations only, the corresponding three-body cluster direct lowest-order terms are shown in Equation (3.11) in [21], and to incorporate these cluster terms, Equation (3.17) was proposed in [21].

In the case of SNM including the tensor and spin-orbit potentials, the corresponding three-body cluster terms are much more complicated. In particular, the spin-orbit correlation function $f_{\mathrm{SO}t}(r_{ij})(\boldsymbol{s} \cdot \boldsymbol{L}_{ij})$ is introduced to describe the correlation between nucleons caused by the nuclear spin-orbit force involving the gradient operator, and it operates on the other correlation functions to generate complicated cluster terms. In this study, for simplicity, we employ an approximation in which the gradient operator $\boldsymbol{L}_{ij}$ involved in f_{ij} operates only on the one-body component of the wave function $\Phi_{\mathrm{F}}(x_1, \ldots, x_N)$. In other words, the contribution of $\boldsymbol{L}_{ij}$ in f_{ij} operating on f_{jk} is ignored.

(3c) Furthermore, we include the lowest-order two-particle exchange three-body cluster terms. In the case of PNM with a central force, the corresponding cluster terms are the part of Equation (3.18) in [21] which is proportional to $[l(r_{23})]^2$. Then, the three-body cluster terms which should be added to $E_{\rm TF}/N$ are expressed in Equation (25), with the denominators in the integrands set to zero.

(3d) Moreover, we include the three-body cluster nodal diagrams (separable diagrams) which are of the lowest order (fourth order) in h_{ij}. As pointed out in [22], where the central and tensor components of the two-body nuclear potential are considered for SNM, the contributions of the nodal diagrams are significant. Furthermore, even for PNM with central, tensor, and spin-orbit forces, the nodal diagrams play a crucial role, as reported in [23]. In the current EEF, $E_{\rm TN}/N$ represents the contribution of the corresponding nodal diagrams.

(4) Finally, we introduce the denominators in the integrands of $E_{\rm TS}/N$ in Equation (25) (i.e., $S_{cn}(k)/S_{\rm cF}(k)$ and $S_{{\rm cT}n}(k)/S_{\rm cF}(k)$) for the following two reasons.

(4a) Without denominators, $E_{\rm TS}/N$ is a harmful term which approaches negative infinity through the variational procedure. The true EEF must exclude these harmful terms. Therefore, we introduce denominators which transform $E_{\rm TS}/N$ without the denominators into harmless terms, ensuring their finiteness through a variational procedure.

(4b) The introduction of the denominators $S_{cn}(k)/S_{\rm cF}(k)$ or $S_{{\rm cT}n}(k)/S_{\rm cF}(k)$ into $E_{\rm TS}/N$ guarantees inequalities for the structure functions shown in Equations (11)–(19). As shown in the inequalities, the exact structure functions $S_{cn}(k)$ and $S_{{\rm cT}n}(k)$ must be nonnegative, and the true EEF is expected to guarantee the inequalities for the structure functions. In fact, when $S_{cn}(k)$ or $S_{{\rm cT}n}(k)$ approaches zero from the positive side, $E_{\rm TS}/N$ becomes positively large, which is not preferable for minimizing the total energy. Therefore, the structure functions remain positive because of the denominators. Note that the contribution of the denominators corresponds to the fourth- and higher-order cluster terms, and the introduction of the denominators in $E_{\rm TS}/N$ does not affect the three-body cluster terms considered in (3b) and (3c). In fact, for the simplest case of uniform fermion systems, the EEF with the denominator is derived directly through the Fermi hypernetted chain method [4].

As explained in the Introduction, we constructed the EEF for PNM with the two-body central, tensor, and spin-orbit potentials in [23]. The obtained results are in good agreement with the results of the AFDMC calculations. Therefore, in this study, we construct the EEF for SNM with central, tensor, and spin-orbit potentials in a similar manner. The only difference is that in [23], we included a part of the three-body cluster terms where $\boldsymbol{L}_{ij}$ in f_{ij} acts on f_{jk}.

2.2. Results for Symmetric Nuclear Matter with the Argonne v8′ Potential

This subsection shows the numerical results for the energy per nucleon of SNM with the Argonne v8′ potential. The Euler–Lagrange equations for $F_{{\rm C}ts}(r)$, $g_{{\rm T}t}(r)$, and $g_{{\rm SO}t}(r)$ are derived from the EEF (Equation (22)) through the variational procedure and then solved numerically for various densities ρ to obtain the E/N.

Figure 1 shows the energy per nucleon of SNM with the Argonne v8′ potential as a function of ρ. The result with the EEF given in Equation (22) is indicated by red circles. We note that the calculated saturation point deviated from the empirical saturation point [26] because the higher-order components in the two-body nuclear force and the three-body nuclear force were not considered in the current calculations.

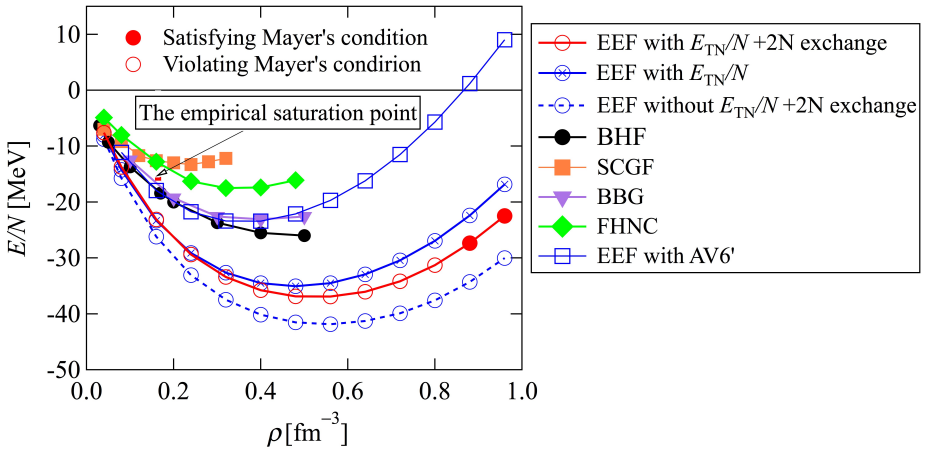

Figure 1. Energy per nucleon of SNM with the Argonne v8′ potential as a function of the density ρ. The results obtained with the BHF, SCGF, BBG, and FHNC methods are also shown in black, dark green, purple, and light green lines, respectively. The open red circles represent the solutions where the Mayer condition was violated, while the filled red circles represent the case where the Mayer condition was satisfied. The open blue squares represent the case using the Argonne v6′ potential. The small red square represents the empirical saturation point [26].

In Figure 1, the filled circles satisfy the Mayer condition, which is expressed as $S_{c1}(0) = 0$, while the open circles violate the Mayer condition. Since the Mayer condition represents the nucleon number conservation, the violation of the Mayer condition would imply the formation of nucleon clusters. Therefore, it is reasonable that the Mayer condition is violated at densities lower than the calculated saturation density where the uniform distribution becomes unstable. At higher densities, on the other hand, the Mayer condition is automatically satisfied, which is also reasonable.

The blue circles with the dashed curve in Figure 1 represent the energy per nucleon without E_{TN}/N. The nodal diagrams show an increase in energy. In contrast, the blue circles with the solid curve represent the energy per nucleon without the lowest-order two-particle exchange three-body cluster terms, which include the spin-orbit correlation function $f_{SOt}(r)$ (i.e., the EEF with $S_{SOF}(k)$ in E_{TS}/N replaced by $3 - 2S_{cF}(k)$). The lowest-order two-particle exchange three-body cluster terms which include the spin-orbit correlation function slightly lowered the total energy per nucleon.

The energies per nucleon of SNM with the Argonne v8′ potential calculated via the Brueckner–Hartree–Fock (BHF), self-consistent Green's function (SCGF), Brueckner–Bethe–Goldstone (BBG) [27], and Fermi hypernetted chain (FHNC) methods [28] are also shown in Figure 1. To the best of our knowledge, results with the AFDMC method are not available. However, our results were lower than these results. This discrepancy can be attributed to the absence of three-body cluster terms where $\boldsymbol{L}_{ij}$ in the spin-orbit operator $f_{SOt}(r_{ij})(\boldsymbol{s} \cdot \boldsymbol{L}_{ij})$ operates on another correlation f_{jk}, as mentioned above. Therefore, inclusion of the cluster terms of this type is urgently required.

Here we note that in the case of the BHF method, the medium effect plays an important role in the saturation, while in the case of the variational method, the higher-order cluster terms are inevitable for reliable results, although the relation between them is rather complicated [4]. In any case, since it is known that the lowest-order cluster variational method is insufficient without any constraints, the inclusion of the various appropriate higher-order cluster terms in the EEF is inevitable to obtain reliable numerical results. It should also be noted that there are no technical difficulties in numerical calculations up to a high density of 1 fm^{-3}. This is one of the advantages of the present variational method.

Finally, the blue open squares in Figure 1 show the energy per nucleon of SNM obtained through the EEF variational method with the Argonne v6′ potential [29]. Here, the Argonne v6′ potential consists of the two-body central and tensor components [30]. Although these components are not equal to those of the Argonne v8′ potential, it can be seen that the two-body spin-orbit force significantly lowers the E/N of SNM, which is qualitatively consistent with other many-body calculations [27]. For a more quantitative discussion, the inclusion of the above-mentioned kinetic energy caused by the correlations is necessary.

The spin-isospin-dependent radial distribution functions, $F_{ts}(r)$, are shown in Figure 2 for ρ = 0.08, 0.56, and 0.96 fm^{-3}, respectively. The $F_{ts}(r)$ values are close to zero at small values of r, owing to the repulsive core of the nuclear potential. As r increases, the even-state distribution functions $F_{10}(r)$ and $F_{01}(r)$ have peaks near $r \sim 1$ fm caused by the attraction of the even-state nuclear force, contrary to the case of the odd-state functions $F_{11}(r)$ and $F_{00}(r)$, where the attraction is weak.

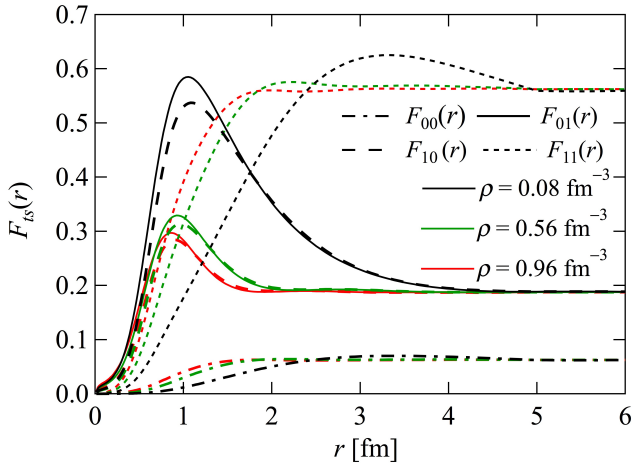

Figure 2. Spin-isospin-dependent radial distribution functions $F_{ts}(r)$ as functions of the distance between nucleons r at $\rho = 0.08$, 0.56, and 0.96 fm^{-3}.

It should be noted that the bump of $F_{11}(r)$ near $r \sim 3$ fm at $\rho = 0.08$ fm^{-3} in Figure 2 is caused by the healing distance. In the current numerical calculations, the solutions to the Euler–Lagrange equations do not converge at some densities without any constraints, and in order to obtain the converged solutions, we introduced the healing distance $r_{\rm h}$ such that at $r = r_{\rm h}$, the auxiliary functions $F_{Cts}(r)$, $g_{{\rm T}t}(r)$, and $g_{{\rm SO}t}(r)$ reduce to their asymptotic values $F_{Cts}(\infty) = (2s+1)(2t+1)/16$ and $g_{{\rm T}t}(\infty) = g_{{\rm SO}t}(\infty) = 0$, respectively. In this study, the healing distance was chosen to be $r_{\rm h} = 5$ fm. On the other hand, $F_{ts}(r)$ at ρ = 0.56 and 0.96 fm^{-3} are similar to each other because they are at the densities higher than the saturation density where the uniform distribution is stable. The amplitudes of $F_{10}(r)$ and $F_{01}(r)$ at $\rho = 0.56$ fm^{-3} near $r \sim 1$ fm are slightly larger than those at $\rho = 0.96$ fm^{-3} because the mean distance between nucleons decreases with an increasing density.

The tensor distribution functions $F_{{\rm T}t}(r)$ and the spin-orbit distribution functions $F_{{\rm SO}t}(r)$ are shown in Figure 3 at ρ = 0.08, 0.56, and 0.96 fm^{-3}. The signs of $F_{\rm T1}(r)$ and $F_{\rm T0}(r)$ are opposite to each other and are determined by the relative phase between $f_{Ct1}(r)$ and $f_{{\rm T}t}(r)$. The extremely large peak of $F_{\rm T0}(r)$ can also be observed near $r \sim 1$ fm at $\rho = 0.08$ fm^{-3}, which is caused by the violation of the Mayer condition (i.e., the formation of deuteron clusters at low densities).

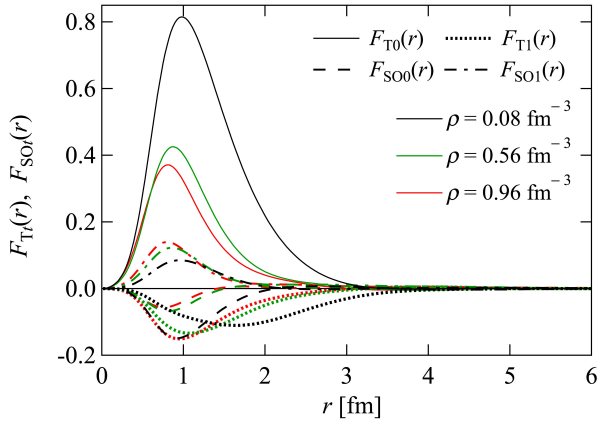

Figure 3. Isospin-dependent tensor distribution functions $F_{Tt}(r)$ and spin-orbit distribution functions $F_{SOt}(r)$ as functions of the distance between nucleons r at ρ = 0.08, 0.56, and 0.96 fm^{-3}.

It should be noted that the present results do not necessarily imply that the deuteron clusters are actually formed; the formation of clusters heavier than deuterons, such as α clusters, is expected in a more realistic case [31]. The present calculations emphasize the formation of deuteron clusters because the Hamiltonian and the many-body method are not suitable for describing the formation of heavier clusters.

Similar to $F_{Tt}(r)$, the signs of $F_{SOt}(r)$ are governed by the phases of $f_{SOt}(r)$ relative to $f_{Ct1}(r)$. Furthermore, as in the case of $F_{ts}(r)$, $F_{Tt}(r)$, and $F_{SOt}(r)$ at ρ = 0.56 fm^{-3} and those at $\rho = 0.96\,\mathrm{fm}^{-3}$, they are close to each other, but the amplitudes of the functions at $\rho = 0.56$ fm^{-3} are slightly larger for the same reasons given above for $F_{10}(r)$ and $F_{01}(r)$. Here, we note that the introduction of the healing distance affects E/N only slightly. E/N is governed by the explicit form of the energy expression.

Figure 4 shows the structure functions $S_{cn}(k)(n = 1 \sim 4)$ at various densities. As mentioned previously, the Mayer condition $S_{c1}(0) = 0$ is violated at relatively low densities. Conversely, as the density increases, $S_{c1}(0)$ approaches zero, thereby satisfying the Mayer condition. In contrast to $S_{c1}(k)$, $S_{cn}(k)$ with $n = 2, 3, 4$ converge to zero as k approaches zero. Additionally, at a given density ρ, the differences between $S_{cn}(k)$ with $n = 2, 3, 4$ are not remarkable.

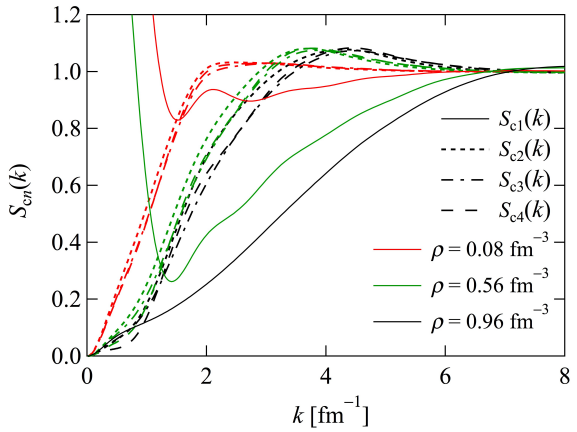

Figure 4. Structure functions $S_{cn}(k)$ as functions of the wave number k at various densities ρ.

The tensor structure functions $S_{cTn}(k)$ are shown in Figure 5. Among these, $S_{cT3}(k)$ is related to pion condensation. In fact, $S_{cT3}(k)$ corresponds to the sum of the isovector spin-longitudinal response given in Equation (5.3) in [32], and the peak of $S_{cT3}(k)$ is a signature of neutral-pion condensation because it minimizes the mean energy of the response (5.10)

in [32]. The pion-condensed phase is established when the energy vanishes. As shown in Figure 5, no substantial peaks were observed in $S_{cT3}(k)$, implying that pion condensation did not occur in the current calculation. This result is reasonable since the three-body nuclear potential was not taken into account in the current calculations; In the case of the Fermi hypernetted chain method, pion condensation did not occur for SNM without the three-body nuclear force, as reported in [32]. Our results agree with these results.

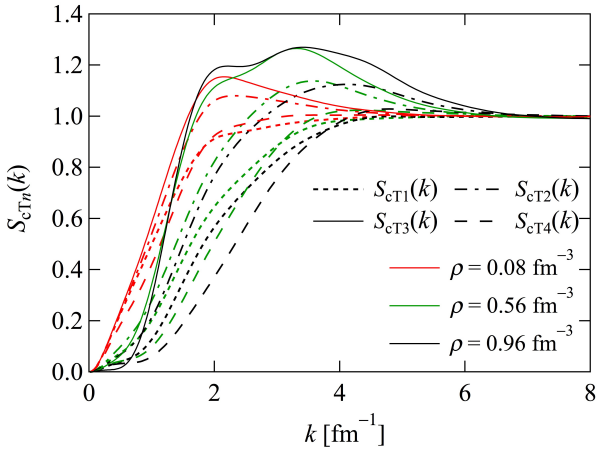

Figure 5. Tensor structure functions $S_{cTn}(k)$ as functions of the wave number k.

Finally, through the procedure of the numerical studies reported above, it was found that E/N for neutron matter with the Argonne v8′ potential given in [23] was inaccurate; the details are provided in Appendix B.

3. Explicit Energy Functional of Pure Neutron Matter at a Finite Temperature

3.1. Construction of the Energy Functional at a Finite Temperature

In this subsection, we report on an extension of our variational theory to nuclear matter at a finite temperature. In the following, we consider PNM, and the Hamiltonian is chosen to be the same as that given in Equation (1). As reported in previous studies, we employed the variational method proposed by Schmidt and Pandharipande [11]. In this method, the free energy per nucleon F/N of PNM at a temperature T is given by

$$\frac{F}{N} = \frac{E_{T0}}{N} - T\frac{S_0}{N}, \tag{34}$$

where E_{T0}/N and S_0/N are the approximate internal energy and approximate entropy per nucleon, respectively.

To construct the approximate internal energy E_{T0}/N using the method by Schmidt and Pandharipande, the energy per nucleon of PNM at zero temperature is first obtained as the expectation value of H/N with the Jastrow wave function $\Psi(x_1, \ldots, x_N)$ for PNM; that is, $\langle\Psi|H|\Psi\rangle/\langle\Psi|\Psi\rangle$. In general, $\langle\Psi|H|\Psi\rangle/\langle\Psi|\Psi\rangle$ is then cluster-expanded, typically using the Fermi hypernetted chain technique to obtain the energy per neutron of PNM E_J/N, which includes the Slater function $l(k_{Fn}r)$ with $k_{Fn} = (3\pi^2\rho)^{1/3}$. In the method proposed by Schmidt and Pandharipande, the one-body kinetic energy $3/5E_F$ in E_J/N is replaced by

$$\frac{E_{T1}}{N} = \frac{1}{\pi^2\rho}\int_0^\infty n(k)\frac{\hbar^2k^2}{2m}k^2dk. \tag{35}$$

In addition, the Slater functions appeared in E_J/N are replaced by

$$l(r,T) = \frac{1}{\pi^2\rho}\int_0^\infty n(k) j_0(kr) k^2 dk \tag{36}$$

to obtain the approximate internal energy E_{T0}/N, where $n(k)$ is the averaged occupation probability of quasi-neutron states:

$$n(k) = \left\{1 + \exp\left[\frac{\varepsilon(k) - \mu_0}{k_B T}\right]\right\}^{-1}. \tag{37}$$

In Equation (37), $\varepsilon(k) = \hbar^2 k^2/(2m^*)$ denotes the quasi-neutron energy, and m^* denotes the quasi-neutron effective mass. In addition, μ_0 in Equation (37) is determined to satisfy the following normalization condition:

$$\rho = \frac{1}{\pi^2}\int_0^\infty n(k) k^2 dk. \tag{38}$$

Furthermore, the approximate entropy per neutron S_0/N is given by

$$\frac{S_0}{N} = -\frac{k_B}{\pi\rho}\int_0^\infty \{[1-n(k)]\ln[1-n(k)] + n(k)\ln n(k)\} k^2 dk, \tag{39}$$

Subsequently, the total free energy F/N is minimized with respect to the effective mass m^*.

This method was originally based on Landau's Fermi liquid theory at low temperatures and was validated by Mukherjee and Pandharipande [33] using the correlated basis function method. This method has also been used to extend the nuclear EOS by APR to nuclear matter at finite temperatures [10]. Consequently, we employ the method of Schmidt and Pandharipande [11] to extend our variational method to nuclear matter at finite temperatures.

Note that in our method, not all Slater functions are shown explicitly in E/N for PNM. The EEF constructed using our variational method for PNM is analogous to Equation (22), expressed with $F_s(r)$, $F_T(r)$, and $F_{SO}(r)$ or, more precisely, the auxiliary functions $F_{Cs}(r)$, $g_T(r)$, and $g_{SO}(r)$, as for SNM (Equations (6)–(8)). They are originally defined using the general wave function $\Psi(x_1,\ldots,x_N)$ rather than the Jastrow wave function, which is similar to the case of SNM (Equations (3)–(5)). Because the part of the EEF expressed with auxiliary functions includes the Slater functions only implicitly, the Schmidt and Pandharipande method cannot be directly applied to our variational method.

Therefore, in our variational method, we minimize the free energy per neutron with respect to not only the neutron effective mass but also the correlation between neutrons. In other words, the free energy per neutron is minimized with respect to the two-body distribution functions and the effective mass.

In other words, we start with the EEF of PNM at zero temperature, which is expressed by $F_s(r)$, $F_T(r)$, and $F_{SO}(r)$ or, more precisely, the auxiliary functions $F_{Cs}(r)$, $g_T(r)$, and $g_{SO}(r)$. Furthermore, the EEF includes $F_{Fs}(r)$ and $F_{qFs}(r)$, which correspond to $F_{Fts}(r)$ and $F_{qFts}(r)$ for SNM given by Equations (9) and (10), respectively. Because $F_{Fs}(r)$ and $F_{qFs}(r)$ correspond to the following neutron occupation probability $n_0(k) = \Theta(k_F - k)$, we replace $n_0(k)$ with $n(k)$, given by Equation (37), to define the functions at finite temperatures $F_{Fs}(r,T)$ and $F_{qFs}(r,T)$. In addition, $F_s(r)$, $F_T(r)$, and $F_{SO}(r)$ appearing in E/N are replaced by the corresponding functions at finite temperatures $F_s(r,T)$, $F_T(r,T)$, and $F_{SO}(r.T)$. Correspondingly, the auxiliary functions at finite temperatures $F_{Cs}(r,T)$, $g_T(r,T)$, and $g_{SO}(r,T)$ are introduced, as in the zero-temperature case. Furthermore, the structure functions at finite temperatures $S_{cn}(k,T)$ and $S_{cTn}(k,T)$ are defined using the Fourier transforms of

$F_s(r,T)$, $F_T(r,T)$, and $F_{SO}(r.T)$, as in the case at zero temperature. Finally, the one-body kinetic energy $3/5E_F$ is replaced by E_{T1}/N as shown in Equation (35).

Thus, E/N at zero temperature is rewritten as the approximate internal energy per neutron E_{T0}/N, whose explicit expression is given in Appendix C. Using this E_{T0}/N, the free energy per neutron F/N is given by Equation (34) with S_0/N as expressed in Equation (39). Then, for a given ρ and T, F/N is minimized with respect to $F_{Cs}(r,T)$, $g_T(r,T)$, $g_{SO}(r,T)$, and m^*; that is, for a fixed value of m^*, the Euler–Lagrange equations for $F_{Cs}(r,T)$, $g_T(r,T)$, and $g_{SO}(r,T)$ are solved numerically, and then the obtained F/N is minimized with respect to m^*. As mentioned in the Introduction, in [22], we extended the EEF at zero temperature with the central and tensor forces to the finite-temperatures case and obtained reasonable results. In this study, we perform a similar extension for PNM including the spin-orbit force.

Here, we note that, for simplicity, in the two-particle exchange three-body cluster terms, the T dependence is considered only partially, the details of which are explained in Appendix C ($S_{l1}(k)$, $S_{Fa}(k)$, and $S_{Fb}(k)$ in Equations (A52)–(A54)).

3.2. Results for Pure Neutron Matter with the Argonne v8′ Potential

In this subsection, we discuss the numerical results of the thermodynamic quantities and related functions for PNM interacting through the Argonne v8′ potential using our variational method. Figure 6 shows the free energy per neutron F/N of PNM as a function of the neutron number density ρ. Overall, F/N showed reasonable behavior; as T increased, F/N decreased. It should be noted that in the present numerical calculations, we introduced the healing distance as in the case of SNM at zero temperature; otherwise, the solutions for the Euler–Lagrange equations at low densities or high temperatures diverged, violating the Mayer condition. In other words, we imposed that $F_{Cs}(r,T) = F_s(\infty)$, $g_T(r,T) = g_{SO}(r,T) = 0$ at $r \geq r_h$, where r_h was chosen to be 5 fm, as in the case of SNM.

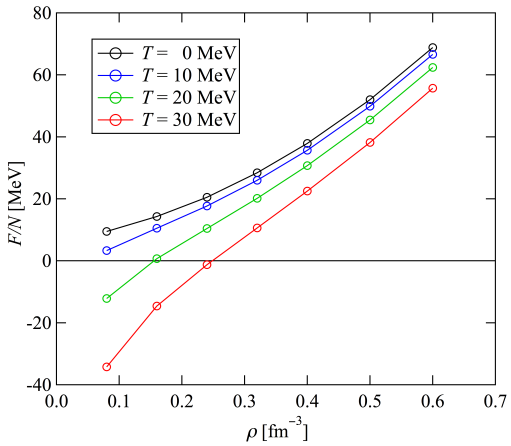

Figure 6. Free energies per neutron F/N of PNM as a function of the neutron number density ρ with the Argonne v8′ potential. The black, blue, green, and red lines represent T = 0, 10, 20, and 30 MeV, respectively.

Figure 7 shows the approximate entropy per neutron S_0/N of PNM as a function of the neutron number density ρ. The behavior of S_0/N was reasonable; it increased with the temperature T and decreased with increasing ρ values. The entropy per neutron S/N, derived from the free energy per neutron F/N, is also shown in this figure. Here, S/N is given by

$$\frac{S}{N} = -\frac{\partial}{\partial T}\left(\frac{F}{N}\right)_\rho. \tag{40}$$

As can be seen in this figure, the S/N value obtained by the thermodynamic relation was in excellent agreement with the approximated S_0/N, thereby indicating the self-consistency of the current calculation.

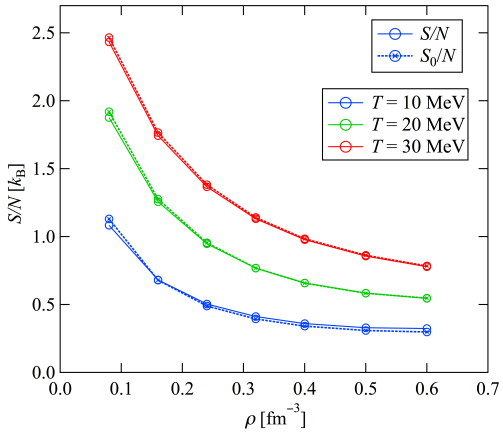

Figure 7. Approximate entropies per neutron S_0/N of PNM as a function of the neutron number density ρ with the Argonne v8′ potential. Entropies per neutron S/N derived from the free energy per neutron F/N by the thermodynamic relation are also shown. Solid lines represent the entropies, while dashed lines represent the approximated entropies. The black, blue, and red lines represent the cases of T = 10, 20, and 30 MeV, respectively.

Figure 8 shows the approximate internal energy per neutron E_{T0}/N as a function of the neutron number density ρ. The behavior of E_{T0}/N was also reasonable; that is, as T increased, E_{T0}/N increased from E/N at zero temperature. Furthermore, E_{T0}/N increased to a greater extent at lower densities. The internal energy per neutron E_T/N, derived from F/N, is shown in this figure. The E_T/N value obtained by the thermodynamic relation was also in excellent agreement with the approximated E_{T0}/N because of the self-consistency of S/N ($E_{T0}/N = F/N + TS_0/N$ and $E_T/N = F/N + TS/N$).

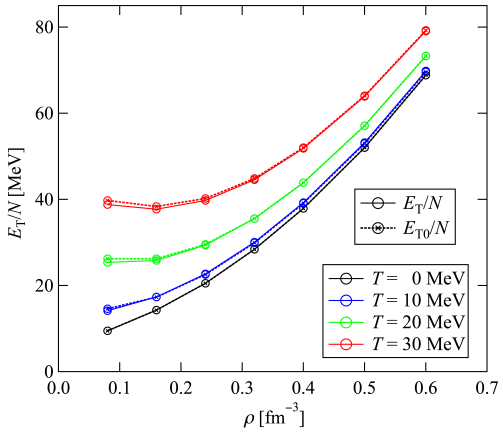

Figure 8. Approximate internal energy per neutron E_{T0}/N of PNM as a function of the neutron number density ρ with the Argonne v8′ potential. The internal energy per neutron E_T/N, derived from the free energy per neutron F/N by the thermodynamic relation, is also shown. The solid lines represent the internal energies, while the dashed lines represent the approximated internal energies. The black, blue, and red lines represent the cases of T = 10, 20, and 30 MeV, respectively.

Figure 9 shows the effective masses of a neutron normalized by the bare neutron mass as a function of the neutron number density ρ. At relatively low densities, reasonable behavior was observed; that is, m^* decreased as ρ increased. Furthermore, m^* approached the value of the bare neutron mass m as T increased. However, as the density increased, m^* reached a minimum value and then increased. This behavior is inconsistent with the

standard results for the nucleon effective mass in nuclear matter with the two-body force, which typically decreases monotonically with the density [34,35]. This implies that as the density increases, it may no longer be appropriate to consider m^* as the effective neutron mass. The physical interpretation of m^* is left for future work.

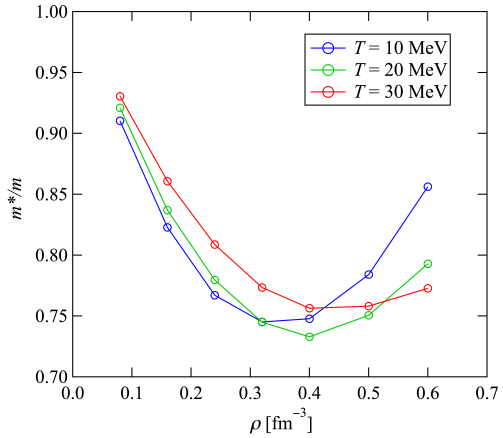

Figure 9. Neutron effective masses normalized by the bare neutron mass as a function of the neutron number density ρ. The blue, green, and red lines represent the results at $T = 10$, 20, and 30 MeV, respectively.

Figure 10 shows spin-dependent radial distribution functions $F_s(r,T)(s = 0,1)$ at temperatures $T = 0$ and 30 MeV and densities ρ = 0.08 and 0.6 fm^{-3}. In the singlet even channel, starting from a small value near the origin, owing to the nuclear repulsive core, $F_0(r,T)$ peaked as r increased, owing to the nuclear attractive force, and then converged to $F_0(\infty,T) = 1/4$. At a density of $\rho = 0.6\,\mathrm{fm}^{-3}$, the T dependence was not strong because of the short mean distance between neutrons. However, at $\rho = 0.08\,\mathrm{fm}^{-3}$, with a longer mean distance, the amplitudes of $F_0(r,T)$ became larger. For the triplet odd channel, $F_1(r,T)$ had no peaks because the attractive component was absent in the nuclear force. The bumps on $F_1(r,T)$ at $\rho = 0.08\,\mathrm{fm}^{-3}$ correspond to the tendency to violate the Mayer condition. This tendency was emphasized at the finite temperature of T = 30 MeV.

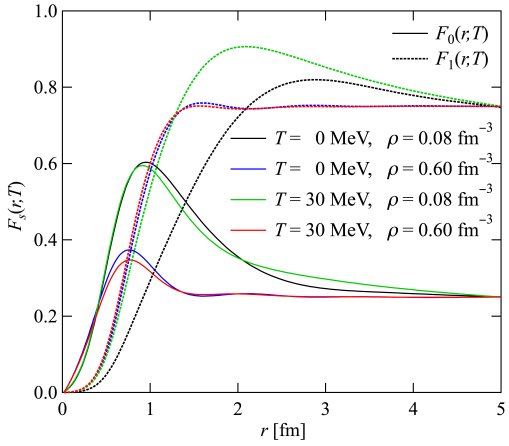

Figure 10. Spin-dependent radial distribution functions $F_s(r,T)$ for PNM at zero ($T = 0$ MeV) and finite temperatures ($T = 30$ MeV). The results at $\rho = 0.08\,\mathrm{fm}^{-3}$ and $\rho = 0.6\,\mathrm{fm}^{-3}$ are shown.

Figure 11 shows the tensor distribution functions $F_\mathrm{T}(r,T)$ and spin-orbit distribution functions $F_\mathrm{SO}(r,T)$ at temperatures $T = 0$ and 30 MeV and densities $\rho = 0.08$ and $0.6\,\mathrm{fm}^{-3}$. As mentioned in the context of SNM, the signs of $F_\mathrm{T}(r,T)$ and $F_\mathrm{SO}(r,T)$ were determined by the phases of the tensor and spin-orbit correlations relative to the central correlations between neutrons, respectively. At the density $\rho = 0.6\,\mathrm{fm}^{-3}$, the peaks of $F_\mathrm{T}(r,T)$ and

$F_{SO}(r,T)$ were at $r \sim 1$ fm, whose T dependence was not so strong. On the other hand, for $\rho = 0.08\,\mathrm{fm}^{-3}$, the average distance between neutrons increased, and the amplitude of $F_T(r,T)$ increased with the temperature, as in the case of $F_s(r,T)$.

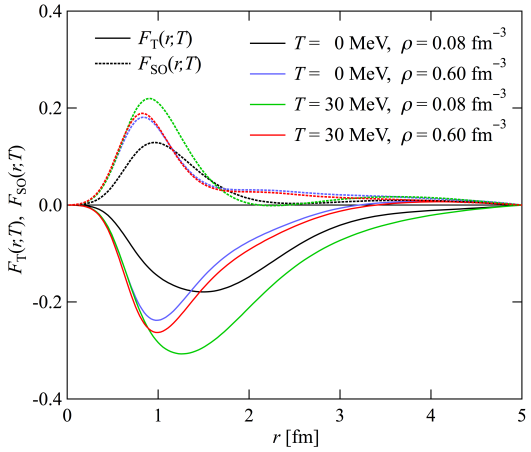

Figure 11. Tensor distribution functions $F_T(r,T)$ and spin-orbit distribution functions $F_{SO}(r,T)$ for PNM at zero ($T = 0$ MeV) and finite temperatures ($T = 30$ MeV). The results at ρ = 0.08 and ρ = 0.6 fm^{-3} are shown.

Figure 12 shows structure functions $S_{cn}(k,T)$ at temperatures $T = 0$ and 30 MeV with densities $\rho = 0.08$ and $0.6\,\mathrm{fm}^{-3}$. At a density $\rho = 0.08\,\mathrm{fm}^{-3}$, the Mayer condition was largely violated even at zero temperature, which may be related to the S-wave pairing instability [36], since the phase transition of PNM to a superfluid is expected at subnuclear densities. To confirm this consideration, it will be necessary to extend our variational method to treat the pairing phase, which will be a future problem. At $T = 30$ MeV, the violation of the Mayer condition increased. At the density $\rho = 0.6\,\mathrm{fm}^{-3}$, a slight violation of the Mayer condition remained for both the zero-temperature and finite-temperature cases. This was mainly due to the introduction of the healing distance.

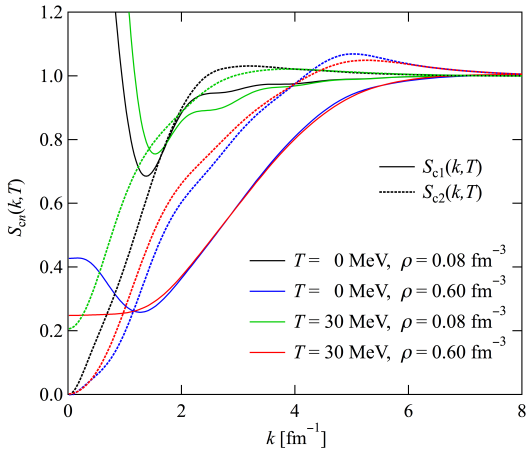

Figure 12. Structure functions $S_{cn}(k,T)$ for PNM at zero ($T = 0$ MeV) and finite temperatures ($T = 30$ MeV). The results at $\rho = 0.08\,\mathrm{fm}^{-3}$, and $\rho = 0.6\,\mathrm{fm}^{-3}$ are shown.

Figure 13 shows tensor structure functions $S_{cTn}(k,T)$ at temperatures $T = 0$ and 30 MeV with densities $\rho = 0.08$ and 0.6 fm^{-3}. In contrast to $S_{c1}(k)$, there was no enhancement near the origin. It is noted that at $\rho = 0.08\,\mathrm{fm}^{-3}$ and $T = 30$ MeV, the values of $S_{cT1}(k,T)$ and $S_{cT2}(k,T)$ were identical at the origin because $S_{c2}(k,T)$ had the same value at the origin. As shown in Equations (A44) and (A45), $S_{cT1}(k,T)$ and $S_{cT2}(k,T)$ differed from $S_{c2}(k,T)$ in $S_T(k,T)$, which vanished at the origin.

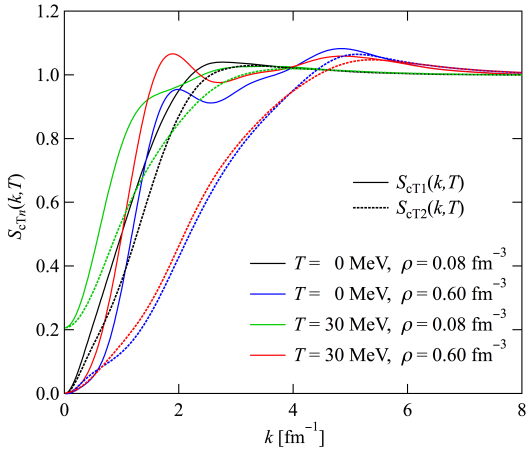

Figure 13. Structure functions $S_{cTn}(k,T)$ for PNM at zero ($T = 0$ MeV) and finite temperatures ($T = 30$ MeV). The results at $\rho = 0.08\,\mathrm{fm}^{-3}$ and $\rho = 0.6\,\mathrm{fm}^{-3}$ are shown.

4. Summary and Concluding Remarks

In this study, we extended the variational method with an explicit energy functional (EEF) in two aspects. First, we considered the spin-orbit component of the nuclear force to construct an EEF for SNM at zero temperature and calculated the energy per nucleon of SNM using the Argonne v8′ two-body nuclear potential. The spin-orbit forces significantly lowered the energy per nucleon of SNM, which is consistent with the results when using other many-body techniques. It was also observed that the energies obtained with our variational method tended to be lower than those obtained with other quantum many-body methods, mainly because of the absence of the effect of the relative orbital angular momentum operator $\boldsymbol{L}_{ij}$ in the spin-orbit correlation function $f_{\mathrm{SO}t}(r_{ij})(\boldsymbol{s}\cdot\boldsymbol{L}_{ij})$ acting on other correlation functions f_{jk}. Consequently, the inclusion of these effects in the EEF is a crucial issue to be studied in the future.

Second, we extended the EEF for PNM at zero temperature, including the spin-orbit force to PNM at finite temperatures, using the method by Schmidt and Pandharipande. With the Argonne v8′ potential as the two-body nuclear force, the calculated free energy per neutron exhibited reasonable behavior as a function of the density and temperature. In addition, thermodynamic self-consistency was validated.

Here, we note that the effect of the spin-orbit force on E/N of PNM depends on the many-body techniques employed. Specifically, the spin-orbit contribution was rather weak in the SCGF, FHNC, and AFDMC methods, while it significantly reduced the energy in the BHF method [37]. In the present variational method, at zero temperature, the E/N of PNM with the Argonne v8′ potential and that with the Argonne v6′ potential [22] were close to each other, as seen in Figure A1; The spin-orbit force slightly decreased the energy at low densities but increased it at higher densities. Therefore, the effect of the spin-orbit force is expected to be less pronounced even for hot PNM, although detailed studies are left for future work.

Furthermore, ensuring the Mayer's condition is important. In the present study, we imposed the Mayer's condition by introducing a healing distance. However, this method is not appropriate because, for example, a bump of $S_{c2}(k)$ at $k \sim 2\,\mathrm{fm}^{-1}$ was found to be exaggerated by the introduction of the healing distance. Therefore, a more sophisticated approach is desirable to guarantee the Mayer's condition.

After refining the EEF for PNM and SNM at zero and finite temperatures with the spin-orbit force, we will next include the $|\boldsymbol{L}_{ij}|^2$ and $(\boldsymbol{s}\cdot\boldsymbol{L}_{ij})^2$ parts of the two-body nuclear force as given in the Argonne v18 potential, and then we will take into account the three-body nuclear force, such as the Urbana IX potential. At this stage, the total energy per

nucleon of SNM at zero temperature must reproduce the empirical saturation point [26]. Finally, the extension of this theory to asymmetric nuclear matter [38] is an important step toward its application to CCSNe.

Author Contributions: Conceptualization, M.T.; methodology, M.T.; software, all authors; formal analysis, all authors; writing—original draft preparation, K.K. and T.O.; writing—review and editing, K.K., T.O. and M.T.; visualization, K.K., T.O. and M.T.; project administration, M.T.; funding acquisition, M.T. All authors have read and agreed to the published version of the manuscript.

Funding: This research was funded by JSPS KAKENHI, Grant No. 20K03979.

Data Availability Statement: The raw data presented in this article will be made available by the authors on request.

Acknowledgments: The authors thank Hajime Togashi for the valuable discussions.

Conflicts of Interest: The authors declare no conflicts of interest.

Appendix A. Energy Expression of Nodal Diagrams in EEF for Symmetric Nuclear Matter at Zero Temperature

In this appendix, we present the explicit functional form of the E_{TN}/N on the right-hand side of Equation (22); in other words, we have

$$\frac{E_{\mathrm{TN}}}{N} = \frac{\hbar^2}{2m}\sum_{n=1}^{6} c_n a_n b_n. \tag{A1}$$

Here, a_n and b_n are expressed as follows:

$$a_1 = 4\pi\rho\int_0^\infty \left\{\left[\frac{dG_{\mathrm{C}}^{\mathrm{I}}(r)}{dr}\right]^2 + 8G_{\mathrm{C}}^{\mathrm{I}}(r)\right\} r^2 dr, \tag{A2}$$

$$\begin{aligned} b_1 = 4\pi\rho\int_0^\infty \Bigg[&\left\{\left[G_{\mathrm{C}}^{\mathrm{I}}(r)\right]^2 + 8\left[g_{\mathrm{T}}^{\mathrm{I}}(r)\right]^2 + \frac{1}{15}\left[g_{\mathrm{SO}}^{\mathrm{I}}(r)\right]^2 (k_{\mathrm{F}}r)^2\right\} \\ &+3\left\{\left[G_{\mathrm{C}}^{\mathrm{II}}(r)\right]^2 + 8\left[g_{\mathrm{T}}^{\mathrm{II}}(r)\right]^2 + \frac{1}{15}\left[g_{\mathrm{SO}}^{\mathrm{II}}(r)\right]^2 (k_{\mathrm{F}}r)^2\right\}\Bigg] r^2 dr, \end{aligned} \tag{A3}$$

$$a_2 = 4\pi\rho\int_0^\infty \left\{\left[\frac{dG_{\mathrm{C}}^{\mathrm{II}}(r)}{dr}\right]^2 + 8G_{\mathrm{C}}^{\mathrm{II}}(r)\right\} r^2 dr, \tag{A4}$$

$$\begin{aligned} b_2 = 4\pi\rho\int_0^\infty \Bigg[&\left\{\left[G_{\mathrm{C}}^{\mathrm{I}}(r)\right]^2 + 8\left[g_{\mathrm{T}}^{\mathrm{I}}(r)\right]^2 + \frac{1}{15}\left[g_{\mathrm{SO}}^{\mathrm{I}}(r)\right]^2 (k_{\mathrm{F}}r)^2\right\} \\ &+2\left\{\left[G_{\mathrm{C}}^{\mathrm{II}}(r)\right]^2 + 8\left[g_{\mathrm{T}}^{\mathrm{II}}(r)\right]^2 + \frac{1}{6}\left[g_{\mathrm{SO}}^{\mathrm{II}}(r)\right]^2 (k_{\mathrm{F}}r)^2\right\}\Bigg] r^2 dr, \end{aligned} \tag{A5}$$

$$a_3 = 4\pi\rho\int_0^\infty \left[\frac{dG_{\mathrm{C}}^{\mathrm{III}}(r)}{dr}\right]^2 r^2 dr. \tag{A6}$$

$$b_3 = 4\pi\rho\int_0^\infty \left\{\left[G_{\mathrm{C}}^{\mathrm{II}}(r)\right]^2 + 8\left[g_{\mathrm{T}}^{\mathrm{II}}(r)\right]^2 + \frac{2}{15}\left[g_{\mathrm{SO}}^{\mathrm{II}}(r)\right]^2 (k_{\mathrm{F}}r)^2\right\} r^2 dr, \tag{A7}$$

$$a_4 = 4\pi\rho \int_0^\infty \left[\left\{ \frac{1}{3}\left[\frac{dH_{C1}(r)}{dr}\right]^2 + \left[\frac{dH_{C0}(r)}{dr}\right]^2 \right\} + 6G_T^{II}(r) + \frac{1}{10}\left[\frac{dg_{SO}^{II}(r)}{dr}\right]^2 (k_F r)^2 \right] r^2 dr, \tag{A8}$$

$$b_4 = 4\pi\rho \int_0^\infty \left[G_C^{III}(r)\right]^2 r^2 dr, \tag{A9}$$

$$a_5 = 4\pi\rho \int_0^\infty \left[\frac{dg_{SO}^{I}(r)}{dr}\right]^2 (k_F r)^2 r^2 dr, \tag{A10}$$

$$b_5 = 4\pi\rho \int_0^\infty \left[\left\{ \left[G_C^{I}(r)\right]^2 + 8\left[g_T^{I}(r)\right]^2 + \frac{109}{1680}\left[g_{SO}^{I}(r)\right]^2 (k_F r)^2 \right\} + 3\left\{ \left[G_C^{II}(r)\right]^2 + 8\left[g_T^{II}(r)\right]^2 + \frac{109}{1680}\left[g_{SO}^{II}(r)\right]^2 (k_F r)^2 \right\} \right] r^2 dr, \tag{A11}$$

$$a_6 = 4\pi\rho \int_0^\infty \left[\frac{dg_{SO}^{II}(r)}{dr}\right]^2 (k_F r)^2 r^2 dr, \tag{A12}$$

$$b_6 = 4\pi\rho \int \left[\left\{ \left[G_C^{I}(r)\right]^2 + 8\left[g_T^{I}(r)\right]^2 + \frac{109}{1680}\left[g_{SO}^{I}(r)\right]^2 (k_F r)^2 \right\} + 5\left\{ \left[G_C^{II}(r)\right]^2 + 8\left[g_T^{II}(r)\right]^2 + \frac{433}{2800}\left[g_{SO}^{II}(r)\right]^2 (k_F r)^2 \right\} \right] r^2 dr. \tag{A13}$$

In the above expressions, we have

$$G_{ts}(r) = F_{Cts}(r) - F_{Fts}(r), \tag{A14}$$

$$G_C^{I}(r) = \frac{1}{3}G_{11}(r) - G_{10}(r) + \frac{1}{3}G_{01}(r) - G_{00}(r), \tag{A15}$$

$$G_C^{II}(r) = \frac{1}{9}G_{11}(r) - \frac{1}{3}G_{10}(r) - \frac{1}{3}G_{01}(r) + G_{00}(r), \tag{A16}$$

$$G_C^{III}(r) = \frac{1}{3}G_{11}(r) + \frac{1}{3}G_{10}(r) - G_{01}(r) - G_{00}(r), \tag{A17}$$

$$H_{C1}(r) = \frac{1}{3}G_{11}(r) - G_{01}(r), \tag{A18}$$

$$H_{C0}(r) = \frac{1}{3}G_{10}(r) - G_{00}(r), \tag{A19}$$

$$g_T^{I}(r) = \frac{1}{4}(3g_{T1}(r) + g_{T0}(r)), \tag{A20}$$

$$g_T^{II}(r) = \frac{1}{4}(g_{T1}(r) - g_{T0}(r)), \tag{A21}$$

$$G_T^{I}(r) = \left[\frac{dg_T^{I}(r)}{dr}\right]^2 + \frac{6}{r^2}\left[g_T^{I}(r)\right]^2, \tag{A22}$$

$$G_T^{II}(r) = \left[\frac{dg_T^{II}(r)}{dr}\right]^2 + \frac{6}{r^2}\left[g_T^{II}(r)\right]^2, \tag{A23}$$

$$g_{SO}^{I}(r) = \frac{1}{4}[3g_{SO1}(r) + g_{SO0}(r)], \tag{A24}$$

$$g_{\mathrm{SO}}^{\mathrm{II}}(r) = \frac{1}{4}[g_{\mathrm{SO1}}(r) - g_{\mathrm{SO0}}(r)]. \tag{A25}$$

Finally, c_n in Equation (A1) is given by

$$(c_1, c_2, c_3, c_4, c_5, c_6) = \left(\frac{3}{4}, \frac{9}{4}, \frac{9}{4}, 3, \frac{1}{20}, \frac{3}{20}\right). \tag{A26}$$

Appendix B. Energy per Neutron of Pure Neutron Matter at Zero Temperature with the Spin-Orbit Force

The energy per neutron of pure neutron matter at zero temperature with the Argonne v8′ potential using the EEF variational method reported in [21] was found to be inaccurate because of errors in the numerical code. Figure A1 shows the improved results using the Argonne v8′ two-body nuclear potential. Also shown is E/N, which includes the repulsive part of the Urbana IX three-body nuclear potential [7,8]. These were compared with the results obtained using the AFDMC method both with and without the Urbana IX three-body nuclear potential. This correction led to a slight increase in E/N at high densities with the Argonne v8′ potential only. When the three-body nuclear potential was considered, the deviation in the results became negligible.

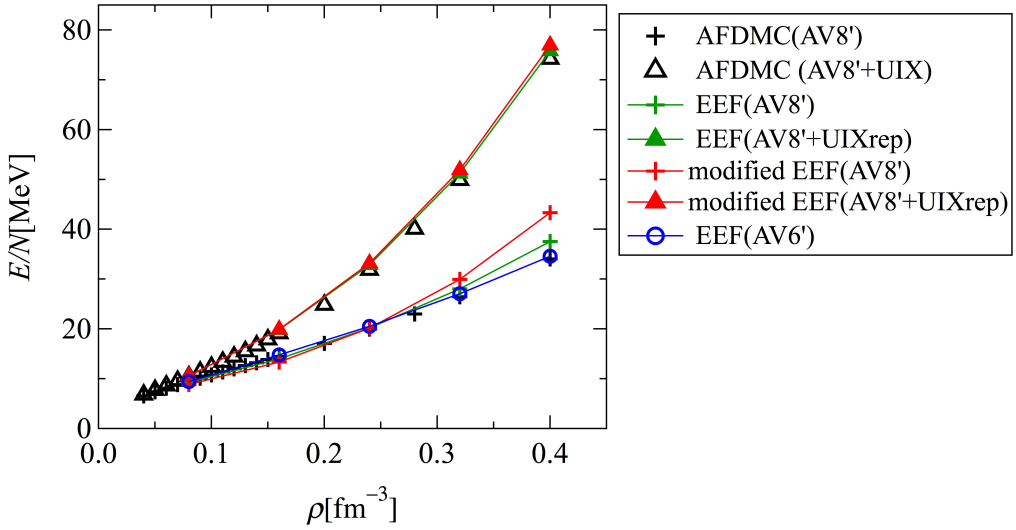

Figure A1. Energy per neutron of PNM with the Argonne v8′ potential as a function of the density ρ. Also shown is the energy per neutron of PNM with the Argonne v8′ potential and the repulsive part of the Urbana IX three-body nuclear potential. They were compared with the results using the AFDMC method. The blue open circles represents the energy per nucleon of PNM with the Argonne v6′ potential [22].

Appendix C. Approximate Internal Energy Expression for Pure Neutron Matter at a Finite Temperature

In this appendix, an explicit expression of the approximate internal energy per neutron E_{T0}/N for PNM is presented:

$$
\begin{aligned}
\frac{E_{\mathrm{T0}}}{N} &= \frac{E_{\mathrm{T1}}}{N} + 2\pi\rho \int_0^\infty \left[\sum_{s=0}^{1} F_s(r,T) V_{\mathrm{C1}s}(r) + F_{\mathrm{T}}(r,T) V_{\mathrm{T1}}(r) + F_{\mathrm{SO}}(r,T) V_{\mathrm{SO1}}(r) \right] r^2 dr \\
&+ \frac{\pi^2\hbar^2\rho}{2m} \int_0^\infty \sum_{s=0}^{1} \left[\frac{1}{F_{\mathrm{C}s}(r,T)} \frac{dF_{\mathrm{C}s}(r,T)}{dr} - \frac{1}{F_{\mathrm{F}s}(r,T)} \frac{dF_{\mathrm{F}s}(r,T)}{dr} \right]^2 F_{\mathrm{C}s}(r,T) r^2 dr \\
&+ \frac{2\pi^2\hbar^2\rho}{m} \int_0^\infty \left[8 \left\{ \left[\frac{dg_{\mathrm{T}}(r,T)}{dr} \right]^2 + \frac{6}{r^2} [g_{\mathrm{T}}(r,T)]^2 \right\} F_{\mathrm{F1}}(r,T) \right. \\
&\left. + \frac{2}{3} \left[\frac{dg_{\mathrm{SO}}(r,T)}{dr} \right]^2 F_{\mathrm{qF1}}(r,T) \right] r^2 dr \\
&- \frac{\hbar^2}{16\pi^2 m\rho} \int_0^\infty \frac{[S_{\mathrm{c1}}(k,T) - S_{\mathrm{ex}}(k,T)][S_{\mathrm{c1}}(k,T) - S_{\mathrm{cF}}(k,T)]^2}{S_{\mathrm{c1}}(k,T)/S_{\mathrm{cF}}(k,T)} k^4 dk \\
&- \frac{\hbar^2}{16\pi^2 m\rho} \int_0^\infty \sum_{n=1}^{2} n \frac{[S_{\mathrm{cT}n}(k,T) - S_{\mathrm{ex}}(k,T)][S_{\mathrm{cT}n}(k,T) - S_{\mathrm{cF}}(k,T)]^2}{S_{\mathrm{cT}n}(k,T)/S_{\mathrm{cF}}} (k,T) k^4 dk \\
&- \frac{\hbar^2}{16\pi^2 m\rho} \int_0^\infty \frac{15}{2} \frac{[S_{\mathrm{c1}}(k,T) - S_{\mathrm{FSO}}(k,T)][S_{\mathrm{SO}}(k,T)]^2}{S_{\mathrm{c1}}(k,T)/S_{\mathrm{cF}}(k,T)} k^4 dk \\
&- \frac{\hbar^2}{16\pi^2 m\rho} \int_0^\infty \frac{15}{2} \frac{[S_{\mathrm{cT2}}(k,T) - S_{\mathrm{FSO}}(k,T)][S_{\mathrm{SO}}(k,T)]^2}{S_{\mathrm{cT2}}(k,T)/S_{\mathrm{cF}}(k,T)} k^4 dk \\
&+ \frac{\hbar^2}{2m} \sum_{m=1}^{3} c_m^{(\mathrm{n})} a_m^{(\mathrm{n})} b_m^{(\mathrm{n})}. \qquad \text{(A27)}
\end{aligned}
$$

Here, E_{T1}/N in the first term on the right-hand side of Equation (A27) is given by Equation (35). In the second term on the right-hand side of Equation (A27), $F_s(r,T)$, $F_{\mathrm{T}}(r,T)$, and $F_{\mathrm{SO}}(r,T)$ are the radial distribution functions, tensor distribution functions, and spin-orbit distribution functions at finite temperatures, respectively, which are defined as ensemble averages as follows:

$$F_s(r,T) = \sum_l \left[\exp\left(-\frac{E_{Nl}}{k_{\mathrm{B}}T} \right) \right] F_{sl}(r) \left[\sum_l \exp\left(-\frac{E_{Nl}}{k_{\mathrm{B}}T} \right) \right]^{-1}, \qquad \text{(A28)}$$

$$F_{\mathrm{T}}(r,T) = \sum_l \left[\exp\left(-\frac{E_{Nl}}{k_{\mathrm{B}}T} \right) \right] F_{\mathrm{T}l}(r) \left[\sum_l \exp\left(-\frac{E_{Nl}}{k_{\mathrm{B}}T} \right) \right]^{-1}, \qquad \text{(A29)}$$

$$F_{\mathrm{SO}}(r,T) = \sum_l \left[\exp\left(-\frac{E_{Nl}}{k_{\mathrm{B}}T} \right) \right] F_{\mathrm{SO}l}(r) \left[\sum_l \exp\left(-\frac{E_{Nl}}{k_{\mathrm{B}}T} \right) \right]^{-1}. \qquad \text{(A30)}$$

Here, $F_{sl}(r,T)$, $F_{\mathrm{T}l}(r,T)$, and $F_{\mathrm{SO}l}(r,T)$ are the radial distribution functions, tensor distribution functions, and spin-orbit distribution functions with the lth quantum state of PNM; that is, we have

$$F_{sl}(r_{12}) \equiv \Omega^2 \sum_{\mathrm{spin}} \int \Psi_l^\dagger(x_1,\ldots,x_N) P_{s12} \Psi_l(x_1,\ldots,x_N) d\boldsymbol{r}_3 \ldots d\boldsymbol{r}_N, \qquad \text{(A31)}$$

$$F_{\mathrm{T}l}(r_{12}) \equiv \Omega^2 \sum_{\mathrm{spin}} \int \Psi_l^\dagger(x_1,\ldots,x_N) S_{\mathrm{T}12} \Psi_l(x_1,\ldots,x_N) d\boldsymbol{r}_3 \ldots d\boldsymbol{r}_N, \qquad \text{(A32)}$$

$$F_{\mathrm{SO}l}(r_{12}) \equiv \Omega^2 \sum_{\mathrm{spin}} \int \Psi_l^\dagger(x_1,\ldots,x_N) (\boldsymbol{L}\cdot\boldsymbol{s})_{12} \Psi_l(x_1,\ldots,x_N) d\boldsymbol{r}_3 \ldots d\boldsymbol{r}_N, \qquad \text{(A33)}$$

where $\Psi_l(x_1,\ldots,x_N)$ is the wave function of the lth quantum state. E_{Nl} in Equations (A28)–(A30) are the energy eigenvalues corresponding to $\Psi_l(x_1,\ldots,x_N)$. The auxiliary functions—that is, the intrinsically central distribution functions $F_{\mathrm{C}s}(r,T)$, the dressed tensor correlation

functions $g_{\mathrm{T}}(r,T)$, and the dressed spin-orbit correlation functions $g_{\mathrm{SO}}(r,T)$ at a finite temperature—are defined as the solutions of the following equations:

$$F_s(r,T) = F_{\mathrm{C}s}(r,T) + 8s[g_{\mathrm{T}}(r,T)]^2 F_{\mathrm{F}s}(r,T) + \frac{2}{3}s[g_{\mathrm{SO}}(r,T)]^2 F_{\mathrm{qF}s}(r,T), \tag{A34}$$

$$F_{\mathrm{T}}(r,T) = 16\left[\sqrt{F_{\mathrm{C1}}(r,T)F_{\mathrm{F1}}(r,T)}g_{\mathrm{T}}(r,T) - [g_{\mathrm{T}}(r,T)]^2 F_{\mathrm{F1}}(r,T)\right] - \frac{2}{3}[g_{\mathrm{SO}}(r,T)]^2 F_{\mathrm{qF1}}(r,T), \tag{A35}$$

$$F_{\mathrm{SO}}(r,T) = -24[g_{\mathrm{T}}(r,T)]^2 F_{\mathrm{F1}}(r,T) + \frac{4}{3}\left[\sqrt{\frac{F_{\mathrm{C1}}(r,T)}{F_{\mathrm{F1}}(r,T)}}g_{\mathrm{T}}(r,T) - \frac{[g_{\mathrm{T}}(r,T)]^2}{4} - g_{\mathrm{T}}(r,T)g_{\mathrm{SO}}(r,T)\right]F_{\mathrm{qF1}}(r,T). \tag{A36}$$

Here, $F_{\mathrm{F}s}(r,T)$ and $F_{\mathrm{qF}s}(r,T)$ are given by

$$F_{\mathrm{F}s}(r,T) = \frac{2s+1}{4}\left[1 + (-1)^s l^2(r,T)\right], \tag{A37}$$

$$F_{\mathrm{qF}s}(r,T) = \frac{2s+1}{4}\left[\frac{1}{3}Qr^2 - (-1)^s r^2 l(r,T)U(r,T)\right], \tag{A38}$$

with

$$l(r,T) = \frac{1}{\pi^2\rho}\int_0^\infty n(k) j_0(kr) k^2 dk, \tag{A39}$$

$$Q = \frac{1}{\pi^2\rho}\int_0^\infty n(k) k^4 dk, \tag{A40}$$

$$U(r,T) = \frac{1}{\pi^2\rho}\int_0^\infty n(k)\frac{j_1(kr)}{kr} k^4 dk. \tag{A41}$$

In Equations (A39)–(A41), $n(k)$ is the averaged occupation probability of single quasi-neutron states, given by Equation (37).

The fifth through eighth terms on the right-hand side of Equation (A27) are expressed using structure functions at finite temperatures, which are defined as follows:

$$S_{\mathrm{c}1}(k,T) \equiv \frac{1}{N}\left\langle\left|\sum_{i=1}^N \exp(i\boldsymbol{k}\cdot\boldsymbol{r}_i)\right|^2\right\rangle_T = 1 + S_1(k,T) + S_0(k,T) \geq 0, \tag{A42}$$

$$S_{\mathrm{c}2}(k,T) \equiv \frac{1}{3N}\left\langle\left|\sum_{i=1}^N \boldsymbol{\sigma}_i \exp(i\boldsymbol{k}\cdot\boldsymbol{r}_i)\right|^2\right\rangle_T = 1 + \frac{1}{3}S_1(k,T) - S_0(k,T) \geq 0 \tag{A43}$$

$$S_{\mathrm{cT}1}(k,T) \equiv \frac{1}{Nk^2}\left\langle\left|\sum_{i=1}^N (\boldsymbol{\sigma}_i\cdot\boldsymbol{k}) \exp(i\boldsymbol{k}\cdot\boldsymbol{r}_i)\right|^2\right\rangle_T = S_{\mathrm{c}2}(k,T) - \frac{1}{3}S_{\mathrm{T}}(k,T) \geq 0, \tag{A44}$$

$$S_{\mathrm{cT}2}(k,T) \equiv \frac{1}{2Nk^2}\left\langle\left|\sum_{i=1}^N (\boldsymbol{\sigma}_i\times\boldsymbol{k}) \exp(i\boldsymbol{k}\cdot\boldsymbol{r}_i)\right|^2\right\rangle_T = S_{\mathrm{c}2}(k,T) + \frac{1}{6}S_{\mathrm{T}}(k,T) \geq 0. \tag{A45}$$

Here, the parentheses with subscript T in the above equations represent the ensemble averages at temperature T, and

$$S_s(k,T) = 4\pi\rho\int_0^\infty [F_s(r,T) - F_s(\infty,T)] j_0(kr) r^2 dr, \tag{A46}$$

$$S_{\mathrm{T}}(k,T) = 4\pi\rho \int_0^\infty F_{\mathrm{T}}(r,T) j_2(kr) r^2 dr, \tag{A47}$$

$$S_{\mathrm{SO}}(k,T) = \frac{4\pi\rho}{\sqrt[3]{3\pi\rho}} \int_0^\infty F_{\mathrm{SO}}(r,T) \frac{j_1(kr)}{r} r^2 dr. \tag{A48}$$

Furthermore, $S_{\mathrm{ex}}(k,T)$ is given by

$$S_{\mathrm{ex}}(k,T) = 3 - 2S_{\mathrm{cF}}(k,T). \tag{A49}$$

In addition, $S_{\mathrm{FSO}}(k,T)$ is given by

$$S_{\mathrm{FSO}}(k,T) = \frac{1}{3} S_{\mathrm{cF}}(k,T) + \frac{2}{3} + \frac{5}{3} S_{\mathrm{l1}}(k) + \frac{10}{3} S_{\mathrm{Fa}}(k) + \frac{2}{3} S_{\mathrm{Fb}}(k), \tag{A50}$$

$$S_{\mathrm{cF}}(k,T) = 1 - 2\pi\rho \int_0^\infty [l(r,T)]^2 j_0(kr) r^2 dr, \tag{A51}$$

$$S_{\mathrm{l1}}(k) = 4\pi\rho \int_0^\infty 9 \left[\frac{j_2(k_{\mathrm{Fn}} r)}{k_{\mathrm{Fn}} r}\right]^2 \frac{j_1(kr)}{kr} r^2 dr, \tag{A52}$$

$$S_{\mathrm{Fa}}(k) = 4\pi\rho \int_0^\infty 9 \left[\frac{j_2(k_{\mathrm{Fn}} r)}{k_{\mathrm{Fn}} r}\right] \left[\frac{j_3(k_{\mathrm{Fn}} r)}{k_{\mathrm{Fn}} r}\right] \frac{j_2(kr)}{k^2} k_{\mathrm{Fn}} r dr, \tag{A53}$$

$$S_{\mathrm{Fb}}(k) = 4\pi\rho \int_0^\infty 9 \left[\frac{j_1(k_{\mathrm{Fn}} r)}{k_{\mathrm{Fn}} r}\right] \left[\frac{j_2(k_{\mathrm{Fn}} r)}{k_{\mathrm{Fn}} r}\right] \frac{j_1(kr)}{k} k_{\mathrm{Fn}} r^2 dr. \tag{A54}$$

Here, $S_{\mathrm{l1}}(k)$, $S_{\mathrm{Fa}}(k)$, and $S_{\mathrm{Fb}}(k)$ are functions related to the two-neutron exchange three-body cluster terms caused by the spin-orbit correlation at zero temperature. It is noted that, for simplicity, the T-dependence in $S_{\mathrm{l1}}(k)$, $S_{\mathrm{Fa}}(k)$, and $S_{\mathrm{Fb}}(k)$ are ignored in the present study, and only $S_{\mathrm{cF}}(k,T)$, given by Equation (A51), depends on T.

Finally, the quantities given in the last term on the right-hand side of Equation (A27) are given by

$$a_1^{(\mathrm{n})} = 4\pi\rho \int_0^\infty \left\{ \left[\frac{dG_{\mathrm{c}}(r,T)}{dr}\right]^2 + 8G_{\mathrm{T}}(r,T) \right\} r^2 dr, \tag{A55}$$

$$a_2^{(\mathrm{n})} = 4\pi\rho (3\pi\rho)^{\frac{2}{3}} \int_0^\infty \left[\frac{dg_{\mathrm{SO}}(r,T)}{dr}\right]^2 r^4 dr, \tag{A56}$$

$$a_3^{(\mathrm{n})} = 4\pi\rho \int_0^\infty \left[\frac{d^2 G_{\mathrm{c}}(r,T)}{dr^2}\right] r^2 dr, \tag{A57}$$

$$b_1^{(\mathrm{n})} = 4\pi\rho \int_0^\infty \left\{ [G_{\mathrm{c}}(r,T)]^2 + 8[g_{\mathrm{T}}(r,T)]^2 + \frac{1}{15} (3\pi\rho)^{\frac{2}{3}} [g_{\mathrm{SO}}(r,T)]^2 r^2 \right\} r^2 dr, \tag{A58}$$

$$b_2^{(\mathrm{n})} = 4\pi\rho \int_0^\infty \left\{ [G_{\mathrm{c}}(r,T)]^2 + 8[g_{\mathrm{T}}(r,T)]^2 + \frac{109}{1680} (3\pi\rho)^{\frac{2}{3}} [g_{\mathrm{SO}}(r,T)]^2 r^2 \right\} r^2 dr, \tag{A59}$$

$$b_3^{(\mathrm{n})} = 4\pi\rho \int_0^\infty [g_{\mathrm{SO}}(r,T)]^2 r^4 dr, \tag{A60}$$

$$G_{\mathrm{c}}(r,T) = \frac{1}{3} F_{\mathrm{C1}}(r,T) - F_{\mathrm{C0}}(r,T) - \frac{1}{3} F_{\mathrm{F1}}(r,T) + F_{\mathrm{F0}}(r,T), \tag{A61}$$

$$G_{\mathrm{T}}(r,T) = \left[\frac{dg_{\mathrm{T}}(r,T)}{dr}\right]^2 + \frac{6}{r^2} [g_{\mathrm{T}}(r,T)]^2, \tag{A62}$$

$$\left(c_1^{(\mathrm{n})}, c_2^{(\mathrm{n})}, c_3^{(\mathrm{n})}\right) = \left(\frac{3}{4}, \frac{1}{20}, \frac{56}{9}\right). \tag{A63}$$

References

1. Burgio, G.F.; Schulze, H.-J.; Vidana, I.; Wei, J.-B. Neutron stars and the nuclear equation of state. *Prog. Part. Nucl. Phys.* **2021**, *120*, 103879. [CrossRef]
2. Janka, H.-T.; Langanke, K.; Marek, A.; Pinedo, G.M.; Müller, B. Theory of core-collapse supernovae. *Phys. Rep.* **2007**, *442*, 38–74. [CrossRef]
3. Lattimer, J.M. Neutron Stars and the Nuclear Matter Equation of State. *Ann. Rev. Nucl. Part. Sci.* **2021**, *71*, 433–464. [CrossRef]
4. Clark, J.W. Variational theory of nuclear matter. *Prog. Part. Nucl. Phys.* **1979**, *2*, 89–199. [CrossRef]
5. Akmal, A.; Pandharipande, V.R.; Ravenhall, D.G. Equation of State of nucleon matter and neutron star structure. *Phys. Rev. C* **1998**, *58*, 1804–1828. [CrossRef]
6. Wiringa, R.B.; Stoks, C.G.J.; Schiavilla, R. Accurate nucleon-nucleon potential with charge-independent breaking. *Phys. Rev. C* **1995**, *51*, 38–51. [CrossRef]
7. Carlson, J.; Pandharipande, V.R. Three-nucleon interaction in 3-, 4-, and ∞-Body systems. *Nucl. Phys. A* **1983**, *401*, 59–85. [CrossRef]
8. Pudliner, B.S.; Pandharipande, V.R.; Carlson, J.; Wiringa, R.B. Quantum Monte Carlo calculations of A $\leq$ 6 nuclei. *Phys. Rev. Lett.* **1995**, *22*, 4396–4399. [CrossRef] [PubMed]
9. Iwamoto, F.; Yamada, M. Cluster Development Method in the Quantum Mechanics of Many Particle System, I. *Prog. Theor. Phys.* **1957**, *17*, 543–555. [CrossRef]
10. Mukherjee, A. Variational theory of hot nucleon matter. II. Spin-isospin correlations and equation of state of nuclear and neutron matter. *Phys. Rev. C* **2009**, *79*, 045811. [CrossRef]
11. Schmidt, K.E.; Pandharipande, V.R. Variational theory of nuclear matter at finite temperatures. *Phys. Lett. B* **1979**, *87*, 11–14. [CrossRef]
12. Carlson, J.; Gandolfi, S.; Pederiva, F.; Pieper, S.C.; Schiavilla, R.; Schmidt, K.E.; Wiringa, R.B. Quantum Monte Carlo methods for nuclear physics. *Rev. Mod. Phys.* **2015**, *87*, 1067–1118. [CrossRef]
13. Machleidt, R.; Sammarruca, F. Recent advances in chiral EFT based nuclear forces and their applications. *Prog. Part. Nucl. Phys.* **2024**, *137*, 104117. [CrossRef]
14. Lonardoni, D.; Tews, I.; Gandolfi, S.; Carlson, J. Nuclear and neutron-star matter from local chiral interactions. *Phys. Rev. Res.* **2020**, *2*, 022033. [CrossRef]
15. Lattimer, J.M.; Swesty, F.D. A generalized equation of state for hot, dense matter. *Nucl. Phys. A* **1991**, *535*, 331–376. [CrossRef]
16. Shen, H.; Toki, H.; Oyamatsu, K.; Sumiyoshi, K. Relativistic equation of state of nuclear matter for supernova and neutron star. *Nucl. Phys. A* **1998**, *637*, 435–450. [CrossRef]
17. Togashi, H.; Nakazato, K.; Takehara, Y.; Yamamuro, S.; Suzuki, H.; Takano, M. Nuclear equation of state for core-collapse supernova simulations with realistic nuclear forces. *Nucl. Phys. A* **2017**, *961*, 78–105. [CrossRef]
18. Furusawa, S.; Togashi, H.; Nagakura, H.; Sumiyoshi, K.; Yamada, S.; Suzuki, H.; Takano, M. A new equation of state for core-collapse supernovae based on realistic nuclear forces and including a full nuclear ensemble. *J. Phys. G Nucl. Part. Phys.* **2017**, *44*, 094001. [CrossRef]
19. Togashi, H.; Hiyama, E.; Yamamoto, Y.; Takano, M. Equation of state for neutron stars with hyperons using a variational method. *Phys. Rev. C* **2016**, *93*, 035808. [CrossRef]
20. Baym, G.; Furusawa, S.; Hatsuda, T.; Kojo, T.; Togashi, H. New neutron star equation of state with quark-Hadron crossover. *Astrophys. J.* **2019**, *8853*, 42. [CrossRef]
21. Takano, M.; Yamada, M. A Variational Method for Infinite Fermion Systems with Central Forces. *Prog. Theor. Phys.* **1994**, *91*, 1149–1172. [CrossRef]
22. Takano, M.; Kato, K.; Yamada, M. Explicit Energy Functional for Infinite Nuclear Matter with the Tensor Force. *J. Phys. Conf. Seri.* **2014**, *529*, 012025. [CrossRef]
23. Takano, M.; Suzuki, T.; Sakumichi, N. Variational calculations with explicit energy functionals for fermion systems at zero temperature. *J. Phys. Conf. Seri.* **2016**, *702*, 012016. [CrossRef]
24. Gandolfi, S.; Carlson, J.; Reddy, S.; Steiner, A.W.; Wiringa, R.B. The equation of state of neutron matter, symmetry energy and neutron star matter. *Eur. Phys. J. A* **2014**, *50*, 10. [CrossRef]
25. Pudliner, B.S.; Pandharipande, V.R.; Carlson, J.; Pieper, S.C.; Wiringa, R.B. Quantum Monte Carlo calculations of nuclei with $A \leq 7$. *Phys. Rev. C* **1997**, *56*, 1720–1750. [CrossRef]
26. Sorensen, A.; Agarwal, K.; Brown, K.W.; Chajęcki, Z.; Danielewicz, P.; Drischler, C.; Gandolfi, S.; Holt, J.W.; Kaminski, M.; Ko, C.-M.; et al. Dense nuclear matter equation of state from heavy-ion collisions. *Prog. Part. Nucl. Phys.* **2024**, *134*, 104080. [CrossRef]
27. Baldo, M.; Polls, A.; Rios, A.; Schulze, H.J.; Vidana, I. Comparative study of neutron and nuclear matter with simplified Argonne nucleon-nucleon potentials. *Phys. Rev. C* **2012**, *86*, 064001. [CrossRef]
28. Lovato, A.; Benhar, O.; Fantoni, S.; Illarionov, A.Y.; Schmidt, K.E. Density-dependent nucleon-nucleon interaction from three-nucleon forces. *Phys. Rev. C* **2011**, *83*, 054003. [CrossRef]

29. Takano, M. (Department of Physics and Applied Physics, Waseda University, Tokyo, Japan); Yamada, M. (Department of Physics and Applied Physics, Waseda University, Tokyo, Japan). Unpublished work, 2014.
30. Wiringa, R.B.; Pieper, S.C. Evolution of Nuclear Spectra with Nuclear Force. *Phys. Rev. Lett.* **2002**, *89*, 182501. [CrossRef]
31. Typel, S.; Röpke, G.; Klähn, T.; Blaschke, D.; Wolter, H.H. Composition and Thermodynamics of nuclear matter with light clusters. *Phys. Rev. C* **2010**, *81*, 015803. [CrossRef]
32. Akmal, A.; Pandharipande, V.R. Spin-isospin structure and pion condensation in nucleon matter. *Phys. Rev. C* **1997**, *56*, 2261–2279. [CrossRef]
33. Mukherjee, A.; Pandharipande, V.R. Variational theory of hot nuclear matter. *Phys. Rev. C* **2007**, *75*, 035802. [CrossRef]
34. Li, B.-A.; Cai, B.-J.; Chen, L.-W.; Xu, J. Nucleon effective masses in neutron-rich matter. *Prog. Part. Nucl. Phys.* **2018**, *99*, 29–119. [CrossRef]
35. Benhar, O.; Lovato, A.; Camelio, G. Modeling Neutron Star Matter in the Age of Multimessenger Astrophysics. *Astrophys. J.* **2022**, *939*, 52. [CrossRef]
36. Sedrakian, A.; Clark, J.W. Superfluidity in nuclear systems and neutron stars. *Eur. Phys. J. A* **2019**, *55*, 167. [CrossRef]
37. Baldo, M.; Burgio, G.F.; Schulze, H.-J.; Taranto, G. Nucleon effective masses within the Brueckner-Hartree-Fock theory: Impact on stellar neutrino emission. *Phys. Rev. C* **2014**, *89*, 048801. [CrossRef]
38. Takano, M.; Yamada, M. Variational study of asymmetric nuclear matter and a new term in the mass formula. *Prog. Theor. Phys.* **2006**, *116*, 545–571. [CrossRef]